Precambrian Research 216–219 (2012) 208–231

Contents lists available at SciVerse ScienceDirect

Precambrian Research

journal homepage: www.elsevier.com/locate/precamres

A multiple sulfur and organic carbon isotope record from non-conglomeratic sedimentary rocks of the Mesoarchean Witwatersrand Supergroup, South Africa

B.M. Guy[a,*], S. Ono[b], J. Gutzmer[a,c], A.J. Kaufman[d], Y. Lin[b,1], M.L. Fogel[e], N.J. Beukes[a]

[a] Department of Geology, University of Johannesburg, Auckland Park 2006, South Africa
[b] Department of Earth, Atmospheric, and Planetary Sciences, Massachusetts Institute of Technology, 77 Massachusetts Avenue, Cambridge, MA, 02139, USA
[c] Helmholtz-Institute Freiberg for Resource Technology, Halsbrücker Str. 34, 09596 Freiberg, Germany
[d] Department of Geology and Earth System Science Interdisciplinary Center, University of Maryland College Park, MD 20742, USA
[e] Geophysical Laboratory, Carnegie Institution of Washington, 5251 Broad Branch Road, NW, Washington, DC 20015, USA

ARTICLE INFO

Article history:
Received 12 February 2012
Received in revised form 24 June 2012
Accepted 29 June 2012
Available online xxx

Keywords:
Diagenetic pyrite
Mesoarchean
Sulfur mass-independent fractionation
Witwatersrand Supergroup
Anaerobic methanotrophy
Diamictite

ABSTRACT

Multiple sulfur isotope ratios ($^{36}S/^{34}S/^{33}S/^{32}S$) and organic carbon isotope ratios ($^{13}C/^{12}C$) were measured from 198 non-conglomeratic sedimentary samples that were collected from five deep diamond drill-cores that cover the majority of the ca. 2.96–2.82 Ga Witwatersrand Supergroup. $\delta^{13}C_{org}$, $\delta^{34}S_{py}$ and $\Delta^{33}S_{py}$ values of the sample set range from −44.3 to −21.9‰, −3.7 to +16.5‰ and −4.0 to +1.9‰, respectively. These geochemical data vary relative to depositional facies (proximal marine, distal marine and fluvial-dominated) and tectonic setting (trailing margin and foreland basin).

In the trailing margin setting of the ~2.96 Ga Hospital Hill Subgroup, the proximal marine depofacies is characterized by relatively high organic carbon contents (up to 0.9 wt.%) and $\delta^{13}C_{org}$ values around −28‰, in contrast to the distal marine depofacies that yields low organic carbon contents (0.01 wt.%) and high $\delta^{13}C_{org}$ values (up to −22‰). Both depofacies yield low sulfur contents (0.02 wt.‰), a narrow range of $\delta^{34}S$ values (~+3 ± 2‰) and positive $\Delta^{33}S$ values (up to +1.9‰). This data is consistent with photoautotrophic carbon fixation in shallow marine environments and limited organic carbon production/preservation in deeper water settings due to longer transport distances and effective biological degradation (e.g., Fe-reducing microbes). Positive $\Delta^{33}S$ values imply that sulfur was largely derived from a photochemical elemental sulfur reservoir. In the foreland basin tectonic setting of the ~2.94 Ga Government and ~2.92 Ga Jeppestown subgroups, shelf deposits associated with fluvial braidplain depofacies are characterized by ^{13}C-depleted organic carbon (~−44 to −38‰), relatively high sulfur contents (0.2–1.3 wt.%), variable $\delta^{34}S$ values (−3.7 to +16.5‰) and small negative $\Delta^{33}S$ values (~−0.4‰). These data suggest that the microbial community in the fluvial-dominated depofacies may have consisted of photoautotrophs, methanogens, anaerobic methanotrophs and sulfate reducers. Sulfate was derived from a variety of sources that include photochemical, crustal and marine sulfur reservoirs.

The occurrence of three regionally persistent diamictite deposits in the Government Subgroup coincides with the onset of compressional tectonics and development of pyritic shales with highly ^{13}C-depleted organic carbon, suggesting that an increase in continental sulfur flux and methane oxidation may have triggered the Mesoarchean glaciations (drawdown of H_2 and CH_4). However, the link between large $\Delta^{33}S$ anomalies (−4.0 to +1.2‰) and diamictite suggests low levels of atmospheric oxygen and minimal dilution of photochemical signatures.

1. Introduction

The Witwatersrand Supergroup has been the World's premier producer of gold for well over the past century. For the geoscientist, this succession and its lateral correlative, the Mozaan Group of the Pongola Supergroup, contain a bonanza of Earth's earliest biological and climatic indicators, including stromatolites, microbial mats and putative glaciogenic diamictites (Beukes and Lowe, 1989; Beukes and Cairncross, 1991; Young et al., 1998; Noffke et al., 2006). The observation of detrital pyrite and uraninite by miners in the

* Corresponding author. Present address: Advanced Mineralogical Facility, SGS South Africa, 58 Melville Street, Booysens, Johannesburg 2091, South Africa. Tel.: +27 11 681 2509; fax: +27 11 433 3654.
E-mail addresses: bradley.guy@sgs.com, bradguy5@gmail.com (B.M. Guy), sono@mit.edu (S. Ono), j.gutzmer@hzdr.de (J. Gutzmer), kaufman@umd.edu (A.J. Kaufman), yinglin@ustc.edu.cn (Y. Lin), m.fogel@gl.ciw.edu (M.L. Fogel), nbeukes@uj.ac.za (N.J. Beukes).
[1] Present address: School of Earth and Space Sciences, University of Science and Technology of China, 96 Jinzhai Road, Hefei, Anhui 230026, PR China.

0301-9268/$ – see front matter © 2012 Elsevier B.V. All rights reserved.
http://dx.doi.org/10.1016/j.precamres.2012.06.018

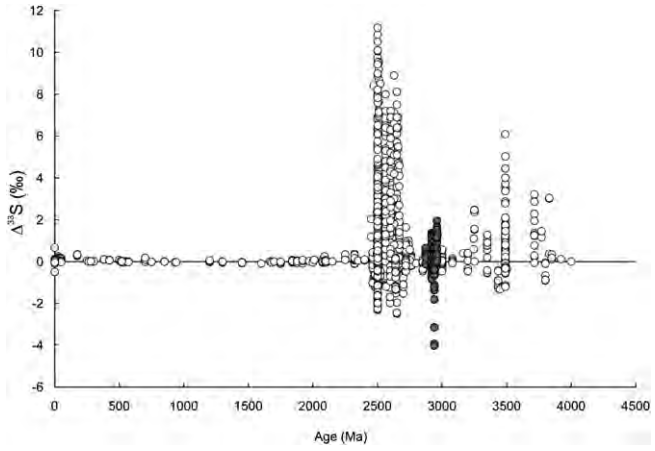

Fig. 1. Age compilation of $\Delta^{33}S$ signatures from sulfur-bearing minerals. New data (grey circles) and previously reported data (white circles).

Data sources: Farquhar et al. (2000, 2002, 2007), Hu et al. (2003), Mojzsis et al. (2003), Savarino et al. (2003), Ono et al. (2003, 2006a,b, 2007, 2009a,b), Bekker et al. (2004), Whitehouse et al. (2005), Papineau et al. (2005, 2007), Johnston et al. (2005, 2006), Ohmoto et al. (2006), Cates and Mojzsis (2006), Kaufman et al. (2007), Philippot et al. (2007), Kamber and Whitehouse (2007), Partridge et al. (2008), Domagal-Goldman et al. (2008), Thomazo et al. (2009) and Hofmann et al. (2009).

Witwatersrand gold mines and the absence of these same detrital minerals in younger fluvial sediments led early workers to suggest that Earth's ancient atmosphere was highly depleted in free oxygen (Cloud, 1972; Grandstaff, 1980; Holland, 1984). Although the geochemical evidence for the onset of oxygenic photosynthesis and oxidative weathering has been reported from rocks as old as 2.78 giga-annum (Ga) (Brocks et al., 1999; Summons et al., 1999, 2006; Anbar et al., 2007), global oxygen levels are thought to have surged sometime between 2.5 and 2.2 Ga, based on the disappearance of detrital pyrite and uraninite, the appearance of Fe-rich paleosols and deposition of manganiferous sediments of the Kalahari manganese field (Holland, 1984; Cairncross et al., 1997; Beukes et al., 2002; Kopp et al., 2005). The exact timing, however, remained elusive until the discovery of mass-independent fractionation of sulfur isotopes (S-MIF)[2] (Farquhar et al., 2000). The disappearance of S-MIF from the rock record at around 2.32 Ga (Bekker et al., 2004; Guo et al., 2009) has been interpreted to reflect the oxidative homogenization of various sulfur reservoirs, i.e., the great oxidation event (GOE) (Fig. 1) (Farquhar et al., 2000; Pavlov and Kasting, 2002; Ono et al., 2003). Since the discovery, secular trends in the magnitude of the Archean $\Delta^{33}S$ signal have been recognized. In this regard, sulfides from Mesoarchean successions display dampened $\Delta^{33}S$ signals (range of ~2‰) in comparison to Paleoarchean and Neoarchean sulfides and sulfates (range of ~12‰) (Fig. 1) (Ohmoto et al., 2006; Ono et al., 2006a; Farquhar et al., 2007; Hofmann et al., 2009). Several hypotheses have been proposed to explain the muted $\Delta^{33}S$ anomalies:

1. an ephemeral oxidation of the anoxic Archean atmosphere (Ono et al., 2006a),
2. an oxic atmosphere since 3.8 Ga, where large $\Delta^{33}S$ signatures represent periods of large volcanic eruptions (Ohmoto et al., 2006),
3. changes in atmospheric chemistry, such as changes in atmospheric source reactions and the development of a thick organic haze (Farquhar et al., 2007; Domagal-Goldman et al., 2008; Thomazo et al., 2009), and
4. the variability of the oxidation state of volcanic sulfur volatiles (SO_2:H_2S) (Halevy et al., 2010).

However, it must be stressed that these discussions have been based on a limited number of bulk rock analyses and were characterized by inadequate constraints on pyrite paragenesis and depositional setting. Consequently, this study was undertaken to address many of these shortcomings and expand the multiple sulfur isotope database. Non-conglomeratic strata of the Witwatersrand Supergroup were specifically targeted since this succession represents the lateral correlative of the diamictite-bearing Mozaan succession measured by Ono et al. (2006a) and because of the preferential accumulation of diagenetic pyrite in argillaceous sedimentary rocks (e.g., Ono et al., 2009a). Furthermore, the stratigraphy, sedimentology and basin architecture of the Witwatersrand Supergroup is well studied and fresh deep-diamond drill cores are readily available. The sampling strategy employed in this contribution was designed to track sulfur isotope variations relative to lateral and vertical changes in the rock record. Both bulk rock and micro-drilling techniques were employed to document mixing trends and small-scale $\Delta^{33}S$ heterogeneity in pyrite. These measurements are complemented by detailed petrographic and chemical analyses of pyrite from the same sample set (Guy et al., 2010). Bulk rock organic carbon concentrations and $\delta^{13}C_{org}$ compositions were also measured to examine S/C relationships (e.g., Berner and Raiswell, 1983) and links between ancient sulfur and organic carbon cycling (e.g., Ono et al., 2006a; Thomazo et al., 2009).

Thus, this contribution presents the results of a multiple sulfur and organic carbon isotope study of non-conglomeratic sedimentary rocks of the Witwatersrand Supergroup and illustrates how isotope compositions of diagenetic pyrite vary systematically with respect to pyrite paragenesis, depositional environment and tectonic setting.

2. Geological background

The Witwatersrand Supergroup and the Mozaan Group represent the oldest known cratonic cover sequences on Earth. The preserved structural remnants outcrop over the central and southeastern portions of the Kaapvaal Craton and together, may have occupied an area in excess of 320,000 km^2 (Fig. 2A) (Beukes and Cairncross, 1991; Nhleko, 2003). Both successions are composed of low-grade (greenschist facies) metamorphosed sandstone, wackestone, siltstone and mudstone, with minor contributions of conglomerate, mafic lava and diamictite (Law and Phillips, 2005). Conventional sedimentary terminology is employed when describing the succession because of the excellent preservation of sedimentary textures (Beukes and Cairncross, 1991; Beukes, 1995). Note that the fine-grained sedimentary rocks of the Witwatersrand Supergroup have suffered considerably less hydrothermal-metasomatic alteration in comparison to the variably altered Au-U conglomeratic facies in the upper parts of the succession (Meyer et al., 1990; Phillips and Law, 2000; Guy, 2012).

[2] S-MIF is a characteristic feature of Archean and early Proterozoic sulfide and sulfate minerals and is thought to have originated from sulfur photochemistry in an Archean atmosphere devoid of oxygen and an ozone shield (Farquhar et al., 2000). Atmospheric model calculations predict that S-MIF can only be preserved when there is an excess of strongly reducing compounds (CH_4 and H_2) in the troposphere and the partial pressure of O_2 is below 10^{-5} times present atmospheric levels (PAL) (Farquhar et al., 2000; Pavlov and Kasting, 2002; Ono et al., 2003; Zahnle et al., 2006). S-MIF refers to the anomalous isotope fractionation that deviates from mass-dependent relationships among $\delta^{33}S$, $\delta^{34}S$ and $\delta^{36}S$ (i.e., $\delta^{33}S = 0.515\ \delta^{34}S$ and $\delta^{36}S = 1.9\ \delta^{34}S$); $\Delta^{33}S$ and $\Delta^{36}S$ are the measures that reflect the deviation of ^{33}S and ^{36}S abundance from that expected from mass-dependent fractionation: $\Delta^{33}S = \ln(\delta^{33}S + 1) - 0.515 \cdot \ln(\delta^{34}S + 1)$ and $\Delta^{36}S = \ln(\delta^{36}S + 1) - 1.9 \cdot \ln(\delta^{34}S + 1)$, where $\delta^{3i}S = {}^{3i}R_{sample}/{}^{3i}R_{VCDT} - 1$, ${}^{3i}R = {}^{3i}S/{}^{32}S$, $i = 33, 34, 36$ and VCDT is the Vienna-Canyon Diablo Troilite reference scale defined as $\delta^{33}S$, $\delta^{34}S$ and $\delta^{36}S$ of IAEA S-1 to be −0.3, 0.100 and −0.6‰, respectively (Ono et al., 2006b).

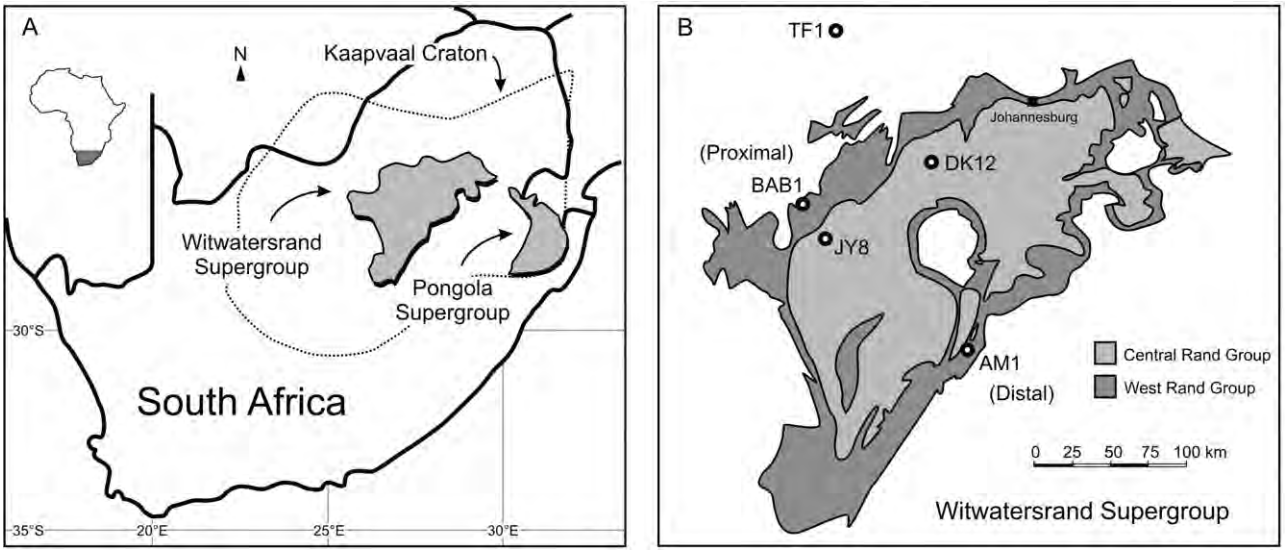

Fig. 2. (A) Geographic position of the Witwatersrand and Pongola supergroups on the Archean Kaapvaal Craton. (B) Locations of drill-cores sampled for this study (TF1, BAB1, JY8, AM1 and DK12).

Sedimentation of the West Rand Group, the lower portion of the Witwatersrand Supergroup, commenced after 2985 ± 14 Ma (youngest detrital zircon age in basal sandstone; Kositcin and Krapez, 2004), whereas the lower age limit of the Mozaan Group is 2985 ± 1 Ma (rhyodacite of the Nsuze Group; Hegner et al., 1994). Sedimentation of the Central Rand Group, the upper portion of the Witwatersrand Supergroup, ended sometime between 2840 ± 3 Ma (detrital xenotime; Kositcin and Krapez, 2004) and 2780 ± 3 Ma (authigenic xenotime; Kositcin et al., 2003). In the Mozaan Group, the upper age limit is defined by the age of an intrusive quartz porphyry sill at 2837 ± 5 Ma (Gutzmer et al., 1999).

The Witwatersrand Supergroup is divided into the lower West Rand Group and the upper Central Rand Group (SACS, 2006; Figs. 2B and 3). The West Rand Group represents an underfilled marine-dominated basin, whereas the Central Rand Group represents an overfilled fluvial-dominated basin (Catuneanu, 2001). The West Rand Group (~5 km thick) is subdivided into the Hospital Hill, Government and Jeppestown subgroups (Fig. 3). The Hospital Hill Subgroup is composed of mature quartz arenite, siltstone-shale, carbonaceous mudstone, magnetite-rich mudstone (magnetic mudstone) and banded iron formation (BIF). Sedimentary beds are laterally extensive suggesting deposition under stable tectonic conditions. In contrast, the Government and Jeppestown subgroups are composed of conglomerate, immature sandstone, quartz arenite, wackestone, siltstone-carbonaceous shale, non-magnetic mudstone (green-colored mudstone devoid of organic matter and magnetite), magnetic mudstone and minor iron formation. Many units contain abundant soft-sediment deformation structures and sharp contacts suggesting rapid deposition and increased tectonic instability relative to the strata of the Hospital Hill Subgroup (Beukes, 1995). A thin amygdaloidal flood basalt (~60 m thick), known as the Crown Lava, occurs in the middle of the Jeppestown Subgroup and has been dated at 2914 ± 8 Ma (Armstrong et al., 1991).

Three prominent sheet-like diamictite units, the Witfontein, Kensington and Lagerspoort members, occur in the Government Subgroup and have been interpreted, along with their Mozaan counterparts, to represent the oldest glacial deposits on Earth (Beukes and Cairncross, 1991; von Brunn and Gold, 1993; Young et al., 1998; Nhleko, 2003). Supporting evidence for a glacial origin includes dropstones, faceted clasts, striated clasts (a clast with possible glacial striations was discovered in this study; see Fig. 11A) and polymictic and exotic clast populations, e.g., granite, gabbro, gneiss, schist, chert, BIF, volcanic and sedimentary rock fragments (Nel, 1935; von Brunn and Gold, 1993; Young et al., 1998). In addition, the diamictite units in the Witwatersrand Supergroup commonly overlie mature inner shelf sandstone beds and exhibit an extensive sheet-like architecture. These features suggest a lack of slope prior to deposition and argue against a tectonically induced debris flow origin, which are generally lobe-shaped and of restricted lateral distribution (Beukes, 1995).

Northern and northeastern source areas were present during the deposition of the Hospital Hill Subgroup, but changed to a northwesterly direction during deposition of the Government and Jeppestown subgroups (Fig. 3) (Beukes, 1995). The sedimentary rocks of the Hospital Hill Subgroup represent inner to outer shelf marine depositional environments, which were deposited in a passive continental or trailing margin tectonic setting with an open ocean to the southeast and to the south (Beukes, 1995; Frimmel et al., 2005). In the Government and Jeppestown subgroups, fluvial braidplain deposits occur in proximal settings, particularly in the northwestern parts of the basin (Watchorn, 1981; Tainton and Meyer, 1990; Meyer et al., 1990; Watchorn and O'Brien, 1991), whereas coeval fine-grained marine sandstones occur in distal settings (Fig. 3). The extensive dispersion of shelf sands during deposition of the Government and Jeppestown subgroups is indicative of a shallow shelf depth profile (Beukes, 1995; Beukes and Cairncross, 1991). The sedimentary rocks of the Government and Jeppestown subgroups have been interpreted to represent either passive margin (Kositcin and Krapez, 2004) or foreland basin deposits (Beukes, 1995; Coward et al., 1995; Catuneanu, 2001; Poujol et al., 2003; Schmitz et al., 2004).

The Central Rand Group (~3 km thick) is subdivided into the Johannesburg and Turffontein subgroups (Fig. 3). In contrast to the West Rand Group, the Central Rand Group is dominated by coarse-grained siliciclastic rocks of fluvial braidplain origin, such as immature sandstone and conglomerate. However, a regionally persistent shale unit, known as the Booysens Formation, is present in the middle of the succession and represents one of the best marker beds in the Central Rand Group (Fig. 3). The argillaceous Booysens Formation probably formed in a shallow marine shelf setting due to a eustatic rise in sea level (Beukes and Nelson, 1995; Karpeta and Els, 1999). A second volcanic unit, the 100–200 m-thick amygdaloidal Bird lava, occurs in the central and eastern parts of the

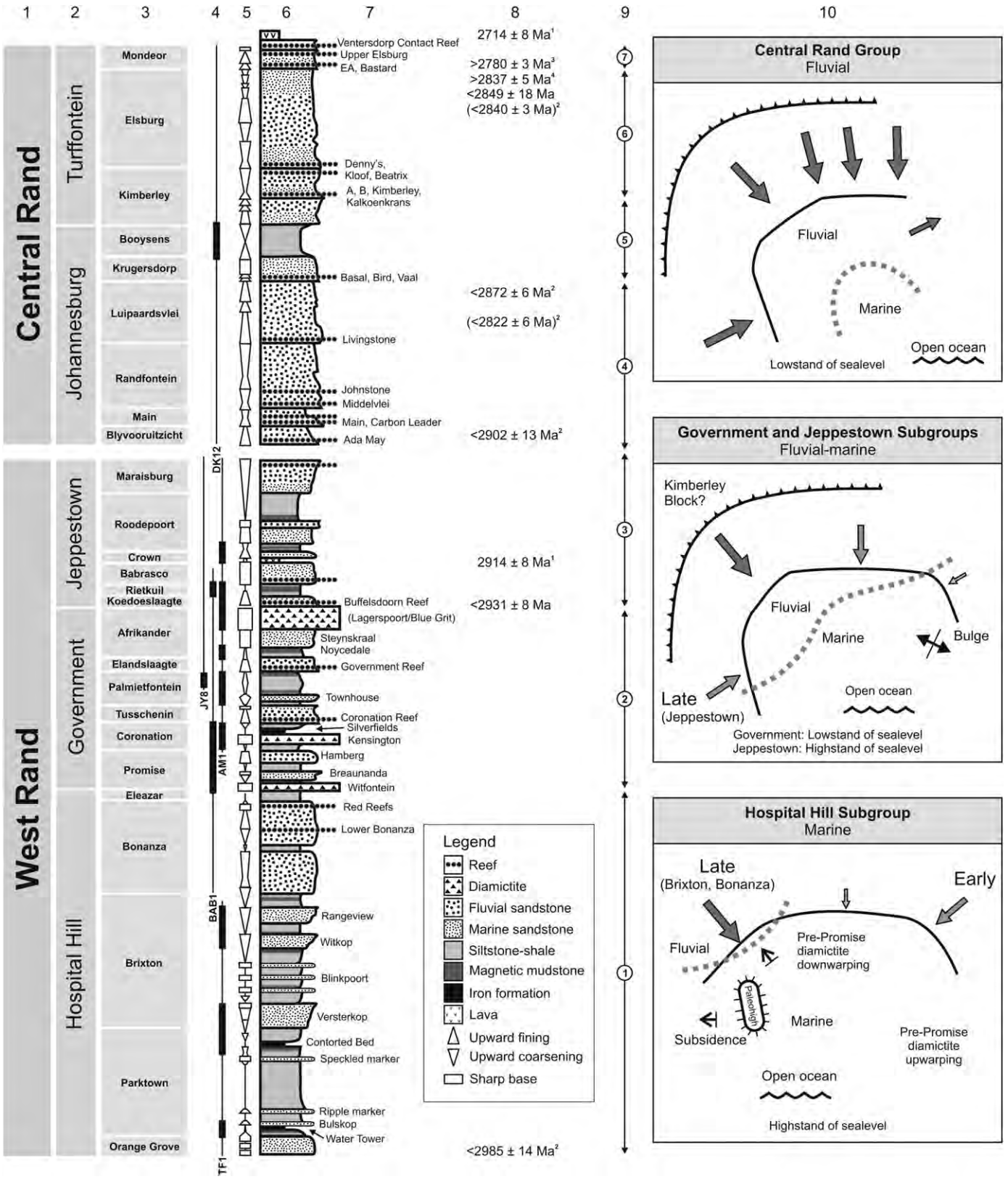

Fig. 3. Lithostratigraphic subdivision of the Witwatersrand Supergroup. Column 1: Groups. Column 2: Subgroups. Column 3: Formations. Column 4: Relative drill-core depths and sampled intervals (black rectangles). Column 5: Genetic successions after Beukes and Nelson (1995). Column 6: Lithology. Column 7: Member/bed/reef. Column 8: Sensitive High-Resolution Ion Microprobe (SHRIMP) U–Pb or Pb–Pb ages after Frimmel et al. (2005), where (1) zircon (Armstrong et al., 1991), (2) zircon and xenotime (Kositcin and Krapez, 2004), (3) authigenic xenotime (Kositcin et al., 2003) and (4) zircon (Gutzmer et al., 1999). Column 9: Supercycles after Beukes and Nelson (1995) where (1) Hospital Hill, (2) Government, (3) Jeppestown, (4) Main, (5) Bird, (6) Gold Estates and (7) Mondeor. Column 10: Schematic reconstruction of the Witwatersrand Basin (modified after Beukes, 1995).

Table 1
Combined paragenetic and morphological classification of pyrite (after Guy et al., 2010).

Detrital pyrite		Diagenetic pyrite		Epigenetic pyrite	
DET-1	Compact, rounded	DIA-1	Microcrystal aggregates	EPI-1	Euhedral crystals
DET-2	Composite lithoclasts	DIA-2	Small euhedral crystals	EPI-2	Overgrowths
		DIA-3	Finely disseminated	EPI-3	Veinlets
		DIA-4	Aggregates	EPI-4	Replacive
		DIA-5	Concretions and nodules	EPI-5	Pyrrhotite and base metal sulfides
		DIA-6	Euhedral to subhedral crystals		
		DIA-7	Dendritic		
		DIA-8	Laths		
		DIA-9	Phyllosilicate pyrite		
		DIA-10	Whiskers		
		DIA-11	Overgrowths		
		DIA-12	Replacive		

basin (Kositcin and Krapez, 2004; SACS, 2006). Deposition of the Central Rand Group took place in a more restricted basin environment in a pericratonic/retroarc foreland basin tectonic setting (Catuneanu, 2001; Schmitz et al., 2004; Frimmel et al., 2005).

3. Materials

3.1. Core samples and sampling strategy

A total of 312 rock samples were collected from 11 formations and five deep diamond drill-cores covering the majority of the stratigraphy of the Witwatersrand succession (TF1, BAB1, JY8, AM1 and DK12) (Fig. 3). Cores TF1, BAB1 and DK12 were drilled in proximal positions in the basin, whereas the cores JY8 and AM1 were drilled in intermediate and distal positions, respectively (Figs. 2B and 3).

The sampling strategy focused on the collection of well preserved mudstones and shales from parasequences that ranged from a few tens of meters to a few hundreds of meters in thickness (Fig. 3). The parasequences grade from deeper and more distal shelf deposits at the base (e.g., BIF and magnetic mudstone) through to inner shelf marine quartz arenites and/or fluvial immature sandstone and conglomerate at the top. The contacts between the parasequences are typically bounded by marine flooding surfaces that are characterized by upward coarsening increments of sedimentation (e.g., Brixton Formation; Fig. 3) or erosional disconformities followed by rapid transgression that are marked by upward fining increments of sedimentation (e.g., Bonanza and Promise formations; Fig. 3). In addition to mudstones and shales, a few samples of other lithotypes were collected, e.g., BIF, wackestone and sandstone. Although veins, faults and diabase contact zones were generally avoided, a few samples were collected for comparison with low grade and unmetamorphosed samples. This systematic and sequence stratigraphic approach removes sampling bias and allows the petrographic and geochemical results to be evaluated in the context of depositional systems tracts, i.e., time-equivalent deposits of offshore distal marine shelf to nearshore and fluvial environments. This approach also facilitates in our understanding of the different depositional environments, since the knowledge of one depofacies contributes to the interpretation of others (Beukes and Buxton, 1992).

Descriptions of the different drill-core (TF1, BAB1, AM1, JY8 and DK12) are as follows:

Drill-core TF1 intersects the majority of the Hospital Hill Subgroup strata in proximal basinal settings (Figs. 2B and 3). Polymodal paleocurrent directions measured from strata of the Hospital Hill Subgroup indicate a marine shelf environment, i.e., on-offshore currents, long-shore currents, tidal currents and storm-generated currents (Camden-Smith, 1980; Beukes, 1995, 1996). Sampled lithologies include supermature quartz arenite, siltstone-carbonaceous shale, carbonaceous mudstone, magnetic mudstone, Fe-carbonate and BIF. Mesoscopic pyrite is extremely rare in both carbonaceous and Fe-rich lithologies, although a pyritic green shale unit occurs below the Contorted Bed BIF.

The proximal BAB1 drill-core intersects strata of the upper Hospital Hill, Government and lower Jeppestown subgroups (Figs. 2B and 3). Unimodal paleocurrent directions, sharp disconformable contacts, upward fining sequences, thick assemblages of poorly sorted feldspathic sandstones and erosively-based gravels are indicative of fluvial braidplain deposits (Watchorn, 1981; Tankard et al., 1982; Beukes, 1995). Sampled lithologies include immature sandstone, wackestone, siltstone-carbonaceous shale, non-magnetic mudstone and diamictite. Magnetic mudstone is very scarce in the BAB1 drill-core (it was only observed in the Palmietfontein Formation). Detrital pyrite grains and diagenetic pyrite segregations are relatively abundant in sandstone and carbonaceous shale, respectively.

In contrast to the BAB1 drill-core, the AM1 drill-core intersects distal strata of the Government and Jeppestown subgroups (Figs. 2B and 3). The bulk of the strata represent marine shelf deposits. Sampled lithologies include quartz arenite, wackestone, non-magnetic mudstone, magnetic mudstone, finely laminated iron formation and diamictite. Carbonaceous mudstone is absent and diagenetic pyrite is scarce (Guy et al., 2010).

Drill-core JY8 intersects strata intermediate between the proximal and distal basinal settings of the Government and Jeppestown subgroups (Figs. 2B and 3). The drill-core contains depositional environments common to both the BAB1 and AM1 drill-cores, such as fluvial braidplain and marine shelf deposits. Only one stratigraphic interval was sampled from the JY8 drill-core, namely the Palmietfontein Formation in the middle part of the Government Subgroup. Sampled lithologies include wackestone, non-magnetic mudstone and magnetic mudstone. Carbonaceous mudstone and mesoscopic pyrite is absent in the sampled interval.

Drill-core DK12 intersects strata belonging to the Central Rand Group (Figs. 2B and 3). Although most of the succession is composed of sandstone and conglomerate that formed in fluvial braidplain settings, the sampled section, i.e., the Booysens Formation, is composed of siltstone-shale that was deposited in a shallow marine shelf setting. Sampled lithologies include immature sandstone, wackestone and siltstone intercalated with carbonaceous shale. Mesoscopic pyrite was not observed.

3.2. Pyrite classification

Pyrite is classified into three broad paragenetic categories or associations: detrital (DET), diagenetic (DIA) and epigenetic (EPI) (Table 1; see Guy et al., 2010). Each paragenetic association contains a number of morphological types (e.g., DET-1, DET-2).

The detrital pyrite association (DET) is composed of two types of pyrite, namely compact pyrite grains that have undergone various degrees of rounding (DET-1) and pyrite enclosed in detrital

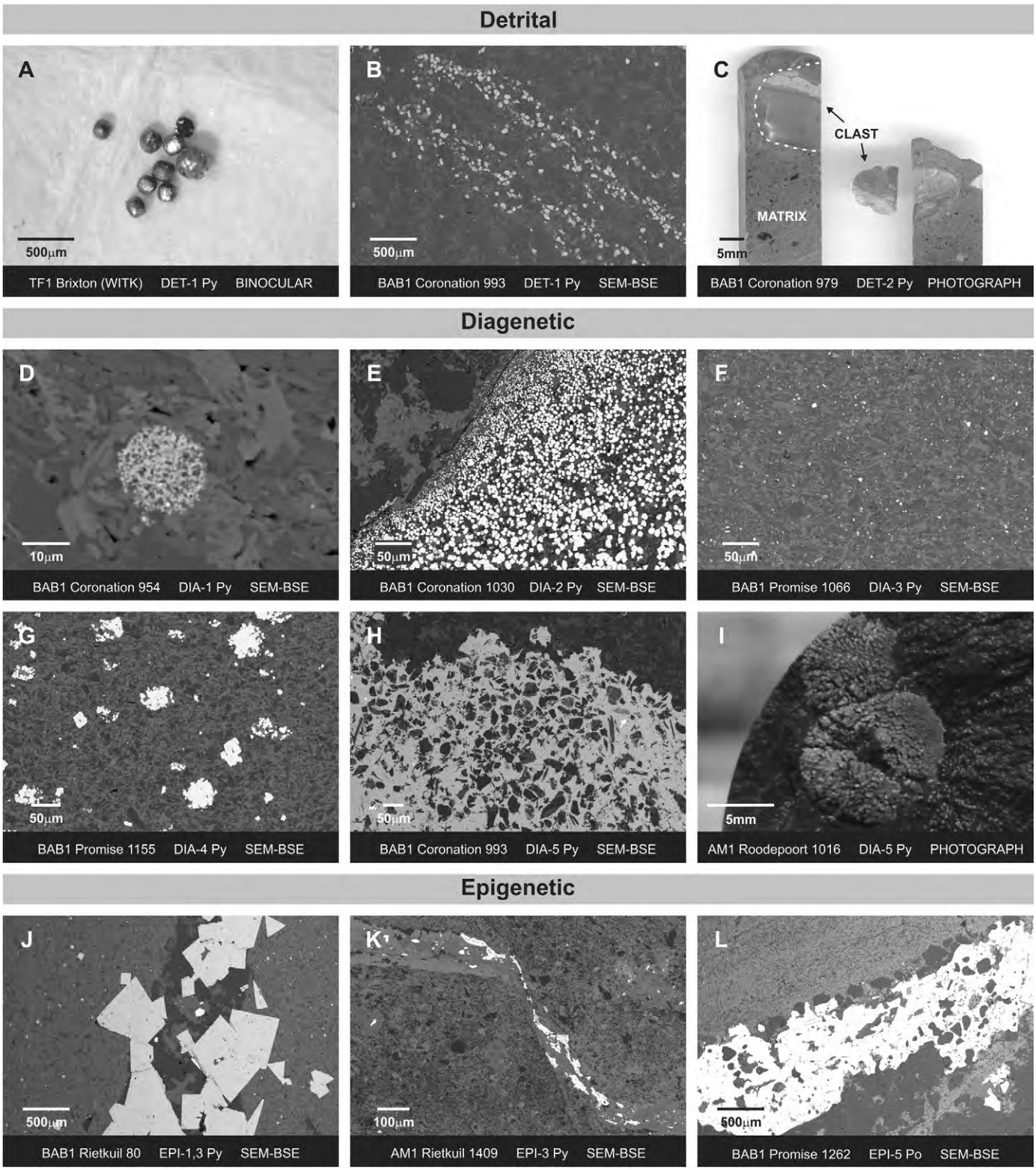

Fig. 4. Representative photomicrographs of detrital, early diagenetic and epigenetic pyrite. Detrital. (A) Detrital compact pyrite grains (DET-1) from the Witkop Member, Brixton Formation. (B) Detrital compact pyrite grains (DET-1) in a heavy mineral lag from the Coronation Formation. (C) Diamictite chert clast (DET-2) with finely disseminated pyrite from the Coronation Formation. Diagenetic. (D) Microcrystal aggregate/framboidal pyrite (DIA-1) in a carbonaceous shale lamina in diamictite from the Coronation Formation. (E) Small euhedral pyrite crystals (DIA-2) in a shale clast from the Coronation Formation. (F) Finely disseminated pyrite (DIA-3) in shale from the Promise Formation. (G) Pyrite aggregates (DIA-4) in a black carbonaceous shale bed from the Promise Formation. (H) Pyrite concretion (DIA-5) in a carbonaceous mudstone lamina in diamictite from the Coronation Formation. (I) Pyrite discs (DIA-5) in non-magnetic mudstone from the Roodepoort Formation. Epigenetic. (J) Euhedral pyrite crystals in a veinlet (EPI-1, 3) from the Rietkuil Formation. (K) Pyrite veinlet (EPI-3) from the Rietkuil Formation. (L) Pervasive pyrrhotite (EPI-5) in a sandstone lamina near a diabase sill from the Promise Formation.

lithoclasts (DET-2). Detrital grains of compact pyrite (DET-1) are readily identified by their rounded morphologies that suggest the erosion and transportation of pyrite crystals (Fig. 4A) (Fleet, 1998). They are commonly associated with other detrital heavy minerals such as zircon, chromite and leucoxene (alteration product after Fe–Ti oxides) (Fig. 4B). Detrital pyrite grains are typically smaller than 0.5 mm and are commonly observed in the BAB1 and DK12 drill-cores, but also in some arenaceous units in the TF1 and JY8 drill-cores. Due to size constraints of the micro-drilling technique (1–2 mm) and the focus on diagenetic pyrite, sulfur isotope analyses were not conducted on detrital pyrite (DET-1). Nevertheless, a few pyrite-bearing diamictite clasts (DET-2) were analyzed for their sulfur isotope compositions (Fig. 4C).

Diagenetic pyrite (DIA) is interpreted to have formed in low temperature environments below the sediment-water interface and between the accumulation and lithification of sedimentary beds. The diagenetic pyrite association contains 12 morphological types (DIA-1 to DIA-12). Pyrite types DIA-1 to DIA-5 represent early diagenetic pyrite (Fig. 4D–I), whereas pyrite types DIA-6 to DIA-12 are interpreted to have formed during the latter stages of diagenesis. The most common types of diagenetic pyrite include μm-sized small euhedral pyrite crystals (DIA-2), mm to cm-sized pyrite segregations (DIA-5) and μm to mm-sized subhedral to euhedral pyrite crystals (DIA-6). Early diagenetic pyrite is relatively abundant in carbonaceous shale beds associated with fluvial braidplain deposits in the BAB1 drill-core, whilst it is virtually absent in marine shelf deposits of the TF1, AM1 and JY8 drill-cores. Early diagenetic pyrite is generally enriched in Co, Ni and As (Guy et al., 2010).

The epigenetic pyrite association (EPI) can be broadly defined as pyrite that formed after deposition and lithification of the country rock. Epigenetic pyrite is commonly associated with diabase sills, faults and shear zones that are linked to regional metamorphic and local hydrothermal events (Fig. 4J–L). The epigenetic pyrite association contains five morphological types (EPI-1 to EPI-5). These include euhedral pyrite crystals (EPI-1), pyrite overgrowths (EPI-2), pyrite veinlets (EPI-3) and replacive pyrite (EPI-4) (Table 1). Note that metamorphic/hydrothermal pyrrhotite and base metal sulfides (EPI-5) are also incorporated into the epigenetic association. The most common types of epigenetic pyrite and pyrrhotite include euhedral pyrite crystals (EPI-1), pyrite veinlets (EPI-3) and irregular pyrrhotite aggregates (EPI-5). Crystal sizes of epigenetic euhedral pyrite (EPI-1) are appreciably larger (mm to cm-sized) than diagenetic euhedral pyrite crystals (DIA-6) (μm to mm-sized) and frequently occur as aggregates along siltstone-shale contacts in permeable silt/sandstone beds. The bulk of epigenetic pyrite is characterized by low trace element concentrations – notably Co. However, when spatially associated with early diagenetic pyrite, epigenetic pyrite is characterized by elevated contents of Ni and/or As (Guy et al., 2010). The sulfur isotope compositions of epigenetic pyrite and pyrrhotite were analyzed for comparison.

4. Analytical methods

The bulk rock sulfur contents of 188 samples were measured by LECO analyses at Set Point Laboratories, South Africa, to select samples for isotope analyses. Selected aliquots of powdered material (1.5 g) were acidified with 6N HCl and agitated overnight, using a rotator, at room temperature to remove carbonate minerals. The residue was washed and dried overnight at 90 °C.

Sulfur isotope analyses ($\delta^{33}S$ and $\delta^{34}S$) were carried out for 162 samples at the Stable Isotope Laboratory at the University of Maryland by a method described in Kaufman et al. (2007). In this first batch, multiple generations of pyrite were analyzed for their sulfur isotope compositions (e.g., detrital, diagenetic and epigenetic pyrite). Of the 162 samples, 120 were measured for bulk rock analyses and 42 were measured for micro-drill analyses. Analyses were performed in duplicate. Separate aliquots of powdered-decarbonated sample material (30 μg to 15 mg) were mixed with proportional amounts of V_2O_5 into small tin cups. The samples were combusted with a pulse of O_2 at 1030 °C and then analyzed by a Eurovector elemental analyzer, in-line with a GV Isoprime mass spectrometer. Uncertainties for $\delta^{34}S$ and $\Delta^{33}S$ are better than 0.3‰.

A further 40 samples, consisting mostly of early diagenetic pyrite, were analyzed for their multiple sulfur isotope compositions ($\delta^{33}S$, $\delta^{34}S$ and $\delta^{36}S$) at the Stable Isotope Geobiology Laboratory at the Massachusetts Institute of Technology. Of the 40 samples, seven were measured for bulk rock analyses and 33 were measured for micro-drill analyses. Sulfur was extracted by conventional Cr reduction and precipitated as Ag_2S (Canfield et al., 1986). The Ag_2S was fluorinated at 300 °C to form SF_6. The SF_6 (6–8 μmol) was purified by a preparatory gas chromatography system similar to the one described in Ono et al. (2006c), and introduced to an isotope ratio mass spectrometer using a dual-inlet mode to measure masses 127, 128, 129, and 131. Reproducibility for complete analysis, from fluorination, GC purification to isotope ratio analysis are 0.1, 0.2 and 0.4‰ (1σ) for $\delta^{33}S$, $\delta^{34}S$ and $\delta^{36}S$, respectively, and 0.01 and 0.1‰ (2σ) for $\Delta^{33}S$ and $\Delta^{36}S$, respectively.

Organic carbon contents and isotopes ($\delta^{13}C_{org}$) were measured from 181 powdered bulk rock samples at the Geophysical Laboratory, Carnegie Institution of Washington (161 samples) and at the Stable Isotope Laboratory at the University of Maryland (20 samples). The carbonate-free bulk rock samples (between 5 and 15 mg) were analyzed for isotope ratios and concentrations for organic carbon using micro-combustion analysis by a Carlo Erba 2500 elemental analyzer (EA) interfaced to a Thermo-Finnigan Delta PlusXL isotope ratio mass spectrometer. Analyses were performed in single and in duplicate. Acetanilide standards (0.15 mg) and blanks were run with each batch of samples and were used to correct for consistent variation in $\delta^{13}C$. Analytical precision for $\delta^{13}C_{org}$ is better than 0.3‰ for samples above 0.03 wt.%, though samples below that level contain systematically larger errors (up to 2.4‰), due to blanks and counting statistics.

Carbonate carbon isotopes ($\delta^{13}C_{carb}$) were measured for nine powdered bulk rock samples at the Department of Geology, University of Cape Town. Powdered carbonate material was treated with 100% phosphoric acid (McCrea, 1950). Values were calibrated using NBS-19 carbonate standard. Reactions involving ankerite took place overnight at 50 °C, whilst those involving siderite took place for four hours at 100 °C. Extracted CO_2 was analyzed using a mass spectrometer. Reproducibility for $\delta^{13}C_{carb}$ is within 0.1‰.

5. Results

The concentrations and isotopic compositions of sulfur and organic carbon are presented in Figs. 5–9 and Table 2. Based on sedimentological, stratigraphic and petrographic observations, the results can be evaluated according to depositional characteristics of the samples. In this regard, three broad depositional facies have been identified, namely proximal marine, distal marine and fluvial-dominated depofacies. Each of these depofacies yields a characteristic relationship between sulfur and organic carbon (Fig. 5). Whilst acknowledging the possibility of minor modification due to greenschist facies metamorphism (e.g., carbon loss and increase of $\delta^{13}C_{org}$ of a few ‰; Hayes, 1983; Strauss et al., 1992; Watanabe et al., 1997; Schidlowski, 2001; Schwab et al., 2005), these relationships are considered as primary or diagenetic in origin largely because of the strict depofacies control, the lack of coexisting carbonate, the presence of low $\delta^{13}C_{org}$ values and the relatively low metamorphic grade of the samples. This excludes samples in

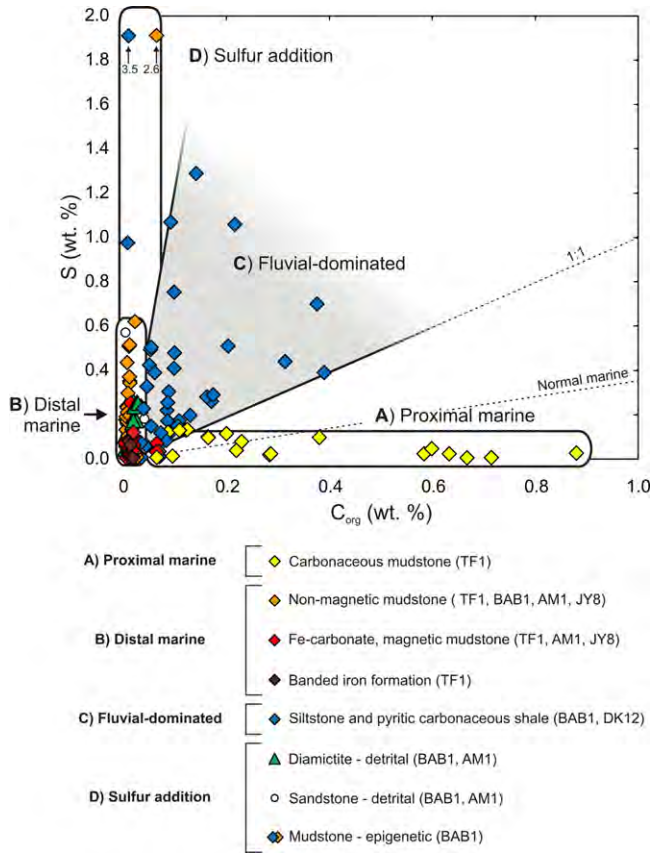

Fig. 5. Plot of bulk rock S versus C_{org} (wt.%) for the (A) proximal marine depofacies, (B) distal marine depofacies, (C) fluvial-dominated depofacies and (D) sulfur addition (detrital and epigenetic pyrite/pyrrhotite). Note that most of the sulfur-rich non-magnetic mudstone samples reflect diagenetic sulfur enrichment (Section 6.2 and Table 2).

contact with diabase sills and fault zones, where the obliteration of primary/diagenetic signatures is evident due to isotope exchange, devolatilization and metasomatic alteration (Fig. 7G). For this reason, a fourth association, defined here as sulfur addition, has been included. This association consists of samples that are dominated by epigenetic pyrite or pyrrhotite, i.e., sulfur unrelated to the depositional and diagenetic environment. Note that samples rich in detrital pyrite would also fall into this association.

5.1. Proximal marine depofacies (low S, high C)

The proximal marine depofacies is represented by carbonaceous mudstone of the Hospital Hill Subgroup (TF1 drill-core) (Figs. 5A and 6 and Table 2). The mudstones exhibit some of the lowest concentrations of sulfur (down to 0.006 wt.%) and the highest concentrations of organic carbon (up to ~0.9 wt.%) (Fig. 6A). S/C ratios average 0.03 in massive carbonaceous mudstone but increase in siltstone-shale due to a decreasing proportion of shale laminae and addition of epigenetic pyrrhotite. $\delta^{13}C_{org}$ values consistently average ~−28‰, irrespective of organic carbon concentrations (Fig. 6A). Average $\delta^{34}S$ and $\Delta^{33}S$ values for rare diagenetic pyrite are +3.1 and +0.9‰, respectively.

5.2. Distal marine depofacies (low S, low C)

The distal marine depofacies is represented by non-magnetic mudstone, magnetic mudstone and BIF from the West Rand Group in the drill-cores TF1, BAB1, AM1 and JY8 (Figs. 5B, 6, 7, 8 and Table 2). These sedimentary rocks are characterized by very low concentrations of organic carbon (average ~0.01 wt.%). The minute amounts of organic carbon yield $\delta^{13}C_{org}$ values enriched in ^{13}C, up to ~−22‰ in BIF (Fig. 6B and Table 2). Diagenetic Fe-carbonate concretions from magnetic mudstone in the lower Parktown Formation contain highly ^{13}C-depleted $\delta^{13}C_{carb}$ values (~−17 to −13‰) and low organic carbon contents (0.02 wt.%) (Fig. 6C and Table 2). Sulfides remain scarce in distal marine settings (0.02 wt.%) but increase below the Water Tower and Contorted Bed BIFs in the Parktown Formation (up to 0.4 wt.%) (Fig. 6D). $\delta^{34}S$ values of diagenetic pyrite average +2.9‰ in the lower Parktown Formation but become more variable in the upper Parktown and Brixton formations (+1.1 to +6.5‰). The ^{34}S-enriched $\delta^{34}S$ values correspond to Fe-carbonate-bearing mudstone and Fe-carbonate-bearing BIF. Significantly, all $\Delta^{33}S$ values in the Hospital Hill Subgroup are positive and increase up to +1.9‰ in BIF.

In the distal marine facies of the Government and Jeppestown subgroups, average sulfur contents are slightly higher compared to the distal marine strata of the Hospital Hill Subgroup (~0.1 wt.%) (Fig. 7F). However, average organic carbon concentrations remain very low (~0.01 wt.%). $\delta^{13}C_{org}$ values of magnetic mudstone range between ~−24 and −26‰, whereas $\delta^{13}C_{org}$ values of non-magnetic mudstone display a wider range between ~−24 and −31‰. Most $\delta^{34}S$ values display a limited range between ~0 and +4‰. The bulk of these samples exhibit positive $\Delta^{33}S$ values, particularly those from ferruginous lithologies (up to +1.2‰) (Fig. 7F). However, negative $\Delta^{33}S$ values were observed from non-magnetic mudstone in the Coronation and Rietkuil formations (down to −0.4 and −0.8‰, respectively). In these two formations, the transition from non-magnetic mudstone to magnetic mudstone/iron formation is associated with a change from negative to positive $\Delta^{33}S$ (Figs. 7E, 8B and D).

5.3. Fluvial-dominated depofacies (S—C covariation)

Braided fluvial deposits in the Witwatersrand succession, *sensu stricto*, are typically composed of immature sandstones with minor conglomerate. The term 'fluvial-dominated' depofacies has been expanded to include shelf siltstone and carbonaceous shale closely associated or interbedded with the fluvial deposits encountered in the Government and Jeppestown subgroups, and in the Central Rand Group (BAB1 and DK12 drill-cores) (Figs. 5C, 7, 8 and Table 2). The shales are characterized by relatively high concentrations of sulfur and organic carbon (up to 1.3 and 0.4 wt.%, respectively) and exhibit weak but positive covariation between sulfur and organic carbon – yielding average S/C ratios between ~1 and 2 (Fig. 5C). Higher S/C ratios in the Promise Formation (~5) correspond to intervals of enhanced diagenetic pyrite mineralization in carbonaceous shale beds (Figs. 4G and 7A). One of the most distinctive traits of the fluvial-dominated depofacies is the occurrence of highly ^{13}C-depleted $\delta^{13}C_{org}$ values (down to −44.3‰). Generally, samples with the most ^{13}C-depleted organic carbon exhibit the highest sulfur contents (Fig. 7A and B). The majority of $\delta^{34}S$ values range between 0 and +5‰, however a small number of samples plot outside this envelope, such as those from the upper Promise Formation (+6.6 to +11.4‰) and those within and above the Coronation diamictite (+16.5 and −3.7‰, respectively) (Fig. 7C and D). Similarly, the largest spread in $\Delta^{33}S$ values for the fluvial-dominated depofacies occurs within and above the Coronation diamictite (+1.2 and −4.0‰, respectively) (Fig. 7C and D). However, most $\Delta^{33}S$ values are negative and average ~−0.4‰. Generally, microdrilled samples of early diagenetic pyrite (e.g., DIA-2, 4 and 5) yield negative $\Delta^{33}S$ values, whereas bulk rock samples with finely disseminated pyrite (DIA-3) yield near-zero or positive $\Delta^{33}S$ values. The Booysens Formation appears to be a transitional depofacies, as it contains geochemical signatures common to both the fluvial-dominated depofacies (S/C covariation and ^{13}C-depleted organic

Table 2
Multiple-sulfur and organic carbon isotope compositions from non-conglomeratic sedimentary strata of the Mesoarchean Witwatersrand Supergroup.

Core	Age (Ma)	Subgroup	Formation	Depth (m)	Lithology	C_{org} (wt.%)	$\delta^{13}C_{org}$ (‰)	$\delta^{13}C_{carb}$ (‰)	S (wt.%)	S/C	Analysis	Method	$\delta^{34}S$ (‰)	$\Delta^{33}S$ (‰)	$\Delta^{36}S$ (‰)	Ni_{py} (ppm)	Textural descriptions	Association
DK12	2870	Johannesburg	Booysens	3296	QTZ-SI	*0.03*	*−26.7*		0.02	0.8								
DK12	2870	Johannesburg	Booysens	3316	ICM	0.07	−31.5		0.06	0.8	SO	Bulk	3.1	−0.1			*DIA-3 Po. EPI-3 Po. EPI-5 Po	MIX
DK12	2870	Johannesburg	Booysens	3325	ICM	0.08	−31.4		0.08	1.0	SO	Bulk	2.9	0.4			*DIA-3 Po. EPI-3 Po. EPI-5 Po	MIX
DK12	2870	Johannesburg	Booysens	3331	ICM	0.07	−31.6		0.12	1.6	SO	Bulk	2.3	0.3			*DIA-3 Po. EPI-5 Po	MIX
DK12	2870	Johannesburg	Booysens	3338	ICM	0.04	−30.7		0.06	1.4	SO	Bulk	2.3	N/A			*DIA-3 Po. EPI-5 Po	MIX
DK12	2870	Johannesburg	Booysens	3342	ICM	*0.07*	*−34.4*		0.01	0.2								
DK12	2870	Johannesburg	Booysens	3350	ICM						SO	Drill	0.7	0.6			*DIA-5 Po	Diagenetic-F
DK12	2870	Johannesburg	Booysens	3357	ICM	0.03	−30.2		0.07	2.2	SO	Bulk	1.9	0.2			*DIA-3 Po. EPI-1 Py. EPI-5 Po	MIX
DK12	2870	Johannesburg	Booysens	3391	QTZ-SI	*0.00*	*−25.7*		0.17	70.6								
DK12	2870	Johannesburg	Booysens	3452	QTZ-SI	*0.01*	*−24.7*		0.22	38.8								
AM1	2920	Jeppestown	Roodepoort	1016	INM	*0.02*	*−27.0*		0.01	0.6	SO	Drill	3.2	1.4		1469	DIA-5 Py	Diagenetic-DM
											SF6	Drill	3.5	1.2	−1.4	441	DIA-5 Py	Diagenetic-DM
AM1	2920	Jeppestown	Roodepoort	1019	IMM	*0.01*	*−25.3*		0.18	17.2	SO	Bulk	1.9	1.1		265	DIA-7 Py	Diagenetic-DM
											SF6	Bulk	0.8	0.9	−1.5	265	DIA-7 Py	Diagenetic-DM
AM1	2920	Jeppestown	Roodepoort	1023	IMM	*0.01*	*−24.9*		0.16	12.0	SO	Bulk	1.7	0.8		327	DIA-6 Py (Incl.-rich in MM). DIA-11 Py	Diagenetic-DM
AM1	2920	Jeppestown	Roodepoort	1026	IMM	*0.01*	*−26.4*		0.17	16.0	SO	Bulk	0.0	0.5		163	DIA-3 Py. DIA-6 Py (Incl.-rich in QTZ). EPI-3 Py	Diagenetic-DM
AM1	2920	Jeppestown	Roodepoort	1029	IMM	*0.01*	*−25.2*		0.09	8.1	SO	Bulk	2.7	N/A		678	DIA-6 Py (Incl.-rich in QTZ)	Diagenetic-DM
AM1	2920	Jeppestown	Roodepoort	1033	IMM	*0.01*	*−25.2*		0.05	8.9	SO	Bulk	2.5	0.2		821	DIA-6 Py (Incl.-rich in QTZ)	Diagenetic-DM
AM1	2920	Jeppestown	Roodepoort	1038	INM	*0.01*	*−25.4*		0.06	8.1	SO	Bulk	2.9	0.3		391	DIA-3 Py. DIA-6 Py (Incl.-rich in QTZ)	Diagenetic-DM
AM1	2920	Jeppestown	Roodepoort	1059	W	*0.02*	*−24.7*		0.01	0.3								
AM1	2920	Jeppestown	Crown	1064	LAVA	*0.02*	*−24.9*		0.01	0.4								
BAB1	2920	Jeppestown	Rietkuil	47	NM	*0.07*	*−26.3*		0.03	0.5	SO	Bulk	N/A	N/A			DIA-6, 7, 9 Py	Diagenetic-DM
BAB1	2920	Jeppestown	Rietkuil	54	IMM	*0.06*	*−26.9*		0.03	0.5	SO	Bulk	N/A	N/A			DIA-3, 9 Py. DIA-6/EPI-1 Py. EPI-3 Py	Diagenetic-DM
BAB1	2920	Jeppestown	Rietkuil	71	Ank-INM	*0.06*	*−27.2*		0.07	1.1	SO	Bulk	N/A	N/A			DIA-3, 6, 9 Py	Diagenetic-DM
BAB1	2920	Jeppestown	Rietkuil	80	NM	*0.06*	*−27.2*		2.58	41.5	SO	Bulk	1.6	0.0			EPI-1 Py. EPI-3 Py	EPI
BAB1	2920	Jeppestown	Rietkuil	98	CM	*0.17*	*−40.2*		0.26	1.5	SO	Bulk	2.0	−0.2			DIA-2, 3, 5, 9, 12 Py. EPI-3 Py	Diagenetic-F
BAB1	2920	Jeppestown	Rietkuil	113	ICM	*0.38*	*−44.3*		0.70	1.9	SO	Bulk	−0.3	−0.5		15,307	DIA-2, 3, 6, 8, 9, 12 Py	Diagenetic-F
BAB1	2920	Jeppestown	Rietkuil	115	ICM	*0.39*	*−44.2*		0.39	1.0	SF6	Drill	2.9	−0.8	−0.6	5799	DIA-1, 2, 3, 4, 5, 6, 8, 9, 12 Py. EPI-3 Py	Diagenetic-F
											SO	Bulk	2.3	−0.3			DET-1 Py. DIA-1, 2, 3, 4, 5, 6, 8, 9, 12 Py. EPI-3 Py	Diagenetic-F
BAB1	2920	Jeppestown	Rietkuil	120	ICM	*0.31*	*−44.1*		0.44	1.4	SO	Bulk	0.6	−0.6			DIA-2, 3, 5, 6, 8, 9, 12 Py. EPI-3 Py	Diagenetic-F
BAB1	2920	Jeppestown	Rietkuil	122	ICM	*0.20*	*−43.0*		0.51	2.5	SF6	Drill	4.1	0.2	−1.0	10,636	DIA-2 Py	Diagenetic-F
											SO	Bulk	3.3	0.0			DIA-1, 2, 3, 5, 6, 9, 12 Py	Diagenetic-F
BAB1	2920	Jeppestown	Rietkuil	123	ICM	*0.16*	*−41.7*		0.28	1.7	SF6	Drill	2.2	−0.4	−1.0	1477	DIA-5 Py	Diagenetic-F
											SO	Bulk	4.2	−0.3			DIA-1, 2, 3, 5, 6, 9 Py	Diagenetic-F
BAB1	2920	Jeppestown	Rietkuil	125	ICM	*0.17*	*−41.8*		0.29	1.7	SF6	Drill	6.6	−0.7	−0.8		DIA-5 Py	Diagenetic-F
											SO	Bulk	6.3	−0.2		4992	DIA-1, 2, 3, 5, 6, 9, 12 Py. EPI-3 Py	Diagenetic-F
BAB1	2920	Jeppestown	Rietkuil	141	ICM	*0.16*	*−38.9*		0.10	0.6	SO	Bulk	1.0	0.3		10,578	DIA-2, 3, 6, 9, 12 Py	Diagenetic-F
AM1	2920	Jeppestown	Rietkuil	1409	INM	*0.01*	*−25.5*		0.01	0.8								
AM1	2920	Jeppestown	Rietkuil	1414	IMM	*0.01*	*−25.0*		0.06	7.9	SO	Bulk	1.4	0.4			DIA-3, 6 Py. EPI-3 Py	Diagenetic-DM
AM1	2920	Jeppestown	Rietkuil	1420	IMM	*0.01*	*−26.5*		0.11	12.1	SO	Bulk	3.0	0.1			*DIA-3 Po. EPI-3 Po	MIX
AM1	2920	Jeppestown	Rietkuil	1428	INM	*0.01*	*−26.7*		0.08	11.4	SO	Bulk	3.9	0.1			*DIA-3, 9, 12 Po. EPI-1, 3, 5 Po	MIX
AM1	2920	Jeppestown	Rietkuil	1434	INM	*0.01*	*−26.3*		0.23	33.1	SO	Bulk	4.2	−0.3			*DIA-3, 5, 9, 12 Po	Diagenetic-DM
											SO	Drill	3.1	−0.2			*DIA-5 Po	Diagenetic-DM
AM1	2920	Jeppestown	Rietkuil	1440	INM	*0.01*	*−30.9*		0.52	42.8	SO	Bulk	4.8	−0.3			*DIA-3, 4?, 9, 12 Po. EPI-3, 5 Po	Diagenetic-DM
AM1	2920	Jeppestown	Rietkuil	1449	INM	*0.02*	*−28.5*		0.17	11.5	SO	Bulk	1.1	−0.2			*DIA-2?, 3, 5?, 6 Po	Diagenetic-DM
AM1	2920	Jeppestown	Rietkuil	1453	INM	*0.01*	*−29.2*		0.34	27.0	SO	Bulk	0.9	−0.8			*DIA-2?, 3, 5?, 9, 12 Po. EPI-5 Po	Diagenetic-DM
AM1	2920	Jeppestown	Rietkuil	1461	INM	*0.01*	*−26.4*		0.10	6.9	SO	Bulk	4.6	−0.2			*DIA-3 Po. DIA-6/EPI-1 Py. EPI-3 Po	AMB
AM1	2920	Jeppestown	Rietkuil	1478	INM	*0.01*	*−25.7*		0.04	4.4								

AM1	2940	Government	Afikander	1692	D	*0.00*	*−24.6*	0.23	65.1	SO	Bulk	1.2	0.1			*DET-2 Po. EPI-5 Po	MIX
AM1	2940	Government	Afikander	1698	D	*0.01*	*−25.1*	0.10	15.7	SO	Bulk	3.7	−0.1			*DET-2 Po. EPI-5 Po	MIX
AM1	2940	Government	Afikander	1708	D	*0.00*	*−25.9*	0.05	17.2								
AM1	2940	Government	Afikander	1715	D					SO	Drill	2.3	0.2			*DET-2/EPI-4 Po	AMB
AM1	2940	Government	Afikander	1721	D					SO	Drill	2.3	0.3			*DET-2 Po	DET
AM1	2940	Government	Afikander	1725	D	*0.01*	*−24.1*	0.16	12.6	SO	Bulk	3.2	−0.1			*DET-2 Po. *DET-2/EPI-4 Po. EPI-5 Po	MIX
										SO	Drill	3.1	0.0			*DET-2 Po/EPI-4 Po	AMB
AM1	2940	Government	Afikander	1735	D	*0.01*	*−27.6*	0.29	20.2	SO	Bulk	2.8	0.0			*DET-2 Po. *DET-2/EPI-4 Po. EPI-5 Po	MIX
AM1	2940	Government	Afrikander	2054	MM	0.02	−26.5	0.17	9.0	SO	Bulk	0.0	1.0			*DIA-3, 5 Po. EPI-3 Po	Diagenetic-DM
										SO	Drill	−1.7	0.7			*DIA-5 Po-Mt	Diagenetic-DM
										SF6	Drill	−2.0	0.6	−1.7		*DIA-5 Po-Mt	Diagenetic-DM
AM1	2940	Government	Afrikander	2057	MM	*0.02*	*−24.7*	0.02	0.9								
AM1	2940	Government	Afrikander	2061	MM	*0.01*	*−24.4*	0.25	17.9	SO	Bulk	1.4	0.9			*DIA-3, 5 Po. EPI-3 Po	Diagenetic-DM
										SF6	Bulk	0.7	0.7	−2.2		*DIA-3, 5 Po. EPI-3 Po	Diagenetic-DM
AM1	2940	Government	Afrikander	2066	MM	*0.01*	*−25.6*	0.05	4.5	SO	Bulk	3.5	1.2			*DIA-3 Po. 30 μm Po agg's	Diagenetic-DM
AM1	2940	Government	Afrikander	2073	MM	0.02	−25.5	0.11	6.0	SO	Bulk	2.6	1.0			*DIA-3 Po. 30 μm Po agg's. EPI-3 Po	Diagenetic-DM
										SF6	Bulk	2.4	0.7	−2.5		*DIA-3 Po. 30 μm Po agg's. EPI-3 Po	Diagenetic-DM
AM1	2940	Government	Afrikander	2080	INM	0.02	−25.2	0.62	28.1	SO	Bulk	0.7	0.6			*DIA-5, 9 Po. EPI-3 Po	Diagenetic-DM
										SO	Drill	0.0	0.7			*DIA-5 Po	Diagenetic-DM
AM1	2940	Government	Palmietfontein	2235	INM	*0.01*	*−25.9*	0.01	1.2								
AM1	2940	Government	Palmietfontein	2250	IMM	*0.01*	*−25.9*	0.08	13.0	SO	Bulk	1.2	0.7			DIA-7 Py. EPI-3 Py	Diagenetic-DM
AM1	2940	Government	Palmietfontein	2263	INM	*0.01*	*−25.2*	0.05	8.7	SO	Bulk	3.1	−0.1			EPI-1 Py	EPI
AM1	2940	Government	Palmietfontein	2270	IMM	*0.01*	*−24.4*	0.01	1.3								
AM1	2940	Government	Palmietfontein	2278	IMM	*0.01*	*−24.4*	0.02	1.6								
AM1	2940	Government	Palmietfontein	2283	IMM	*0.01*	*−26.3*	0.03	3.7	SO	Drill	2.6	0.2			EPI-1 Py	EPI
AM1	2940	Government	Palmietfontein	2382	NM	*0.00*	*−26.1*	0.13	27.1	SO	Bulk	0.1	0.4			EPI-5 Po	EPI
AM1	2940	Government	Palmietfontein	2393	IMM	*0.00*	*−26.2*	0.05	11.5	SO	Bulk	2.6	0.1			*DIA-3 Po. DIA-7 Py. *DIA-12 Po-Mt agg's	Diagenetic-DM
										SO	Drill	1.2	0.4			*DIA-6 Po/EPI-1 Po	AMB
AM1	2940	Government	Palmietfontein	2398	IMM	*0.01*	*−25.6*	0.06	12.1	SO	Bulk	2.8	−0.1			DIA-7 Py? *DIA-12 Po-Mt agg's. EPI-3 Py	MIX
AM1	2940	Government	Palmietfontein	2404	IMM	*0.01*	*−25.6*	0.06	9.9	SO	Bulk	2.6	0.0			*DIA-3 Po. DIA-7 Py	Diagenetic-DM
AM1	2940	Government	Palmietfontein	2408	IMM	*0.01*	*−25.7*	0.11	7.6	SO	Bulk	1.0	0.1			*DIA-5 Po. *DIA-12 Po-Mt agg's	Diagenetic-DM
AM1	2940	Government	Palmietfontein	2415	IMM	0.02	−25.3	0.10	4.9	SO	Bulk	1.7	0.7			DIA-7 Py	Diagenetic-DM
AM1	2940	Government	Palmietfontein	2420	IMM	*0.02*	*−26.4*	0.11	6.9	SO	Bulk	2.9	0.2			*DIA-12 Po-Mt agg's. EPI-3 Py-Po. EPI-5 Po	MIX
AM1	2940	Government	Palmietfontein	2425	MM	*0.01*	*−26.8*	0.12	14.0	SO	Bulk	1.4	0.5			*DIA-5 Po-Py. EPI-1, 3 Po-Py	MIX
										SO	Drill	1.1	0.5			*DIA-5 Po-Py (Py rim)	Diagenetic-DM
										SO	Drill	0.1	0.5			*DIA-5 Po-Py (Po core)	Diagenetic-DM
										SF6	Drill	0.6	0.1	−1.9		*DIA-5 Po-Py (Po core)	Diagenetic-DM
AM1	2940	Government	Palmietfontein	2462	QTZ-W	*0.01*	*−25.6*	0.04	2.5								
AM1	2940	Government	Palmietfontein	2477	NM	*0.01*	*−25.4*	0.44	60.8	SO	Bulk	3.5	0.0			*DIA-3, 5, 9, 12 Po. EPI-3, 5 Po	MIX
AM1	2940	Government	Palmietfontein	2521	INM	*0.01*	*−24.1*	0.30	33.1	SO	Bulk	3.7	0.2			*DIA-3, 5, 9, 12 Po. EPI-3, 5 Po	MIX
AM1	2940	Government	Palmietfontein	2527	INM	*0.01*	*−24.2*	0.07	13.7	SO	Bulk	3.3	0.3			DIA-7 Py. EPI-3 Py	MIX
AM1	2940	Government	Palmietfontein	2531	IMM	*0.01*	*−24.2*	0.02	2.4								
AM1	2940	Government	Palmietfontein	2535	INM	*0.01*	*−26.5*	0.17	25.0	SO	Bulk	3.7	0.0			*DIA-3 Po. EPI-3, 5 Po	MIX
JY8	2940	Government	Palmietfontein	2623	MM	*0.01*	*−26.4*	0.01	1.4								
JY8	2940	Government	Palmietfontein	2628	MM	*0.01*	*−26.1*	0.06	8.4	SO	Bulk	3.7	0.0			DIA-6, 7 Py	Diagenetic-DM
										SO	Drill	2.9	0.6		274	DIA-7 Py	Diagenetic-DM
										SF6	Drill	3.3	0.0	−0.8	274	DIA-7 Py	Diagenetic-DM
JY8	2940	Government	Palmietfontein	2636	MM	*0.01*	*−26.1*	0.07	8.3	SO	Bulk	3.4	−0.2		276	DIA-6, 7 Py	Diagenetic-DM
JY8	2940	Government	Palmietfontein	2646	IMM	*0.01*	*−24.8*	0.01	1.1								
JY8	2940	Government	Palmietfontein	2650	IMM	*0.01*	*−25.7*	0.02	2.1								
JY8	2940	Government	Palmietfontein	2656	IMM	*0.01*	*−29.4*	0.01	0.8								
JY8	2940	Government	Palmietfontein	2660	IMM	*0.01*	*−26.2*	0.09	11.6	SO	Bulk	1.6	−0.1			DIA-3 Py. DIA-6 Py (Incl.-rich). EPI-3 Py	Diagenetic-DM
JY8	2940	Government	Palmietfontein	2667	Ank-MM	*0.00*	*−24.7*	0.07	28.7	SO	Bulk	2.7	0.0			DIA-6, 10 Py	Diagenetic-DM
JY8	2940	Government	Palmietfontein	2676	INM	*0.01*	*−26.4*	0.09	8.6	SO	Bulk	2.8	0.2			DIA-7 Py	Diagenetic-DM
JY8	2940	Government	Palmietfontein	2790	INM	*0.01*	*−25.9*	0.10	12.8	SO	Bulk	2.8	0.1			DIA-6/EPI-1 Py	AMB

Table 2 (*Continued*)

Core	Age (Ma)	Subgroup	Formation	Depth (m)	Lithology	C_{org} (wt.%)	$\delta^{13}C_{org}$ (‰)	$\delta^{13}C_{carb}$ (‰)	S (wt.%)	S/C	Analysis	Method	$\delta^{34}S$ (‰)	$\Delta^{33}S$ (‰)	$\Delta^{36}S$ (‰)	Ni_{py} (ppm)	Textural descriptions	Association
JY8	2940	Government	Palmietfontein	2814	IMM	*0.01*	*−26.4*		0.08	11.6	SO	Bulk	3.9	−0.1			DIA-3, 6 Py. EPI-1, 3 Py	Diagenetic-DM
JY8	2940	Government	Palmietfontein	2827	IMM	*0.00*	*−25.4*		0.08	22.7	SO	Bulk	3.6	0.4			DIA-3, 6, 9 Py. DIA-6/EPI-1 Py	Diagenetic-DM
JY8	2940	Government	Palmietfontein	2832	IMM	*0.01*	*−26.4*		0.06	9.4	SO	Bulk	3.0	−0.2			DIA-3, 6 Py. DIA-6/EPI-1 Py	Diagenetic-DM
JY8	2940	Government	Palmietfontein	2837	INM	*0.02*	*−28.3*		0.10	6.6	SO	Bulk	1.6	0.4			DIA-3, 6 Py. DIA-6/EPI-1 Py	Diagenetic-DM
AM1	2940	Government	Coronation	2805	MM	*0.01*	*−25.4*		0.51	47.0	SO	Bulk	2.1	0.4			DIA-6/EPI-1 Py. EPI-3 Po-Py-Mt. EPI-4, 5 Po	EPI
											SO	Drill	2.2	0.4			DIA-5 Py/EPI-1 Py	AMB
AM1	2940	Government	Coronation	2808	IF	0.01	−25.8		0.35	29.3	SO	Bulk	1.3	0.3			DIA-6 Py. EPI-3, 5 Po	MIX
											SO	Drill	2.2	0.5		153	DIA-6 Py	Diagenetic-DM
AM1	2940	Government	Coronation	2810	D-MM						SO	Drill	0.3	0.6		223	DIA-5 Py	Diagenetic-DM
AM1	2940	Government	Coronation	2811	IF	*0.01*	*−24.7*		0.24	38.7	SO	Bulk	−1.8	0.5			EPI-1, 3 Py	EPI
											SO	Drill	0.6	0.0			EPI-1, 3 Py	EPI
AM1	2940	Government	Coronation	2813	D	*0.01*	*−25.3*		0.09	6.7	SO	Bulk	3.4	0.1			*DET-2/EPI-4 Po. EPI-4 Po (quartz). EPI-5 Po	EPI
											SO	Drill	2.5	0.2			*DET-2/EPI-4 Po	AMB
AM1	2940	Government	Coronation	2817	QTZ	*0.00*	*−25.0*		0.57	143.7	SO	Bulk	1.8	N/A			*DET-1 Po. *DIA-6 Po. EPI-5 Po	MIX
AM1	2940	Government	Coronation	2840	INM	0.01	−25.7		0.21	18.4	SO	Bulk	2.9	0.2			EPI-3, 5 Po	EPI
AM1	2940	Government	Coronation	2843	INM	*0.00*	*−26.4*		0.19	40.8	SO	Bulk	3.5	−0.1			*DIA-3, 5, 9, 12 Po. EPI-5 Po	Diagenetic-DM
AM1	2940	Government	Coronation	2848	INM	*0.01*	*−26.7*		0.21	28.9	SO	Bulk	2.9	−0.1			*DIA-5 Po. EPI-5 Po	MIX
AM1	2940	Government	Coronation	2853	INM	*0.01*	*−28.1*		0.20	17.1	SO	Bulk	3.9	−0.4			*DIA-3, 9, 12 Po. EPI-5 Po	MIX
BAB1	2940	Government	Coronation	914	ICM	0.11	−37.9		0.17	1.6	SO	Bulk	3.2	−0.2			DIA-3, 6, 9, 12 Py. EPI-3 Py	Diagenetic-F
BAB1	2940	Government	Coronation	920	ICM	0.09	−37.9		0.12	1.3	SO	Bulk	3.9	0.0			DIA-3, 6, 9, 12 Py. EPI-3 Py	Diagenetic-F
BAB1	2940	Government	Coronation	925	ICM	0.09	−37.6										DET-1 Py. DIA-2, 3, 6, 9, 12 Py	Diagenetic-F
BAB1	2940	Government	Coronation	930	ICM	0.09	−37.9		0.31	3.5	SO	Bulk	2.0	−0.5			DIA-1, 2, 3, 5, 6, 9, 11, 12 Py	Diagenetic-F
											SF6	Drill	0.0	−2.0	0.3	12,934	DIA-2 Py	Diagenetic-F
											SF6	Drill	−3.7	−1.8	2.0	4739	DIA-5 Py (concretion)	Diagenetic-F
											SO	Drill	−3.4	−3.1		4908	DIA-5 Py (nodule)	Diagenetic-F
											SF6	Drill	−2.7	−4.0	2.2	7417	DIA-5 Py (nodule)	Diagenetic-F
BAB1	2940	Government	Coronation	934	ICM	0.11	−38.2		0.15	1.4	SO	Bulk	4.8	−0.3			DIA-3, 6, 9, 12 Py	Diagenetic-F
BAB1	2940	Government	Coronation	937	ICM	0.12	−38.2		0.13	1.1	SO	Bulk	3.9	−0.2			DIA-3, 6, 9, 12 Py. EPI-3 Py	Diagenetic-F
BAB1	2940	Government	Coronation	941	ICM	0.13	−37.9		0.20	1.5	SO	Bulk	3.2	−0.1			DET-1, 2 Py. DIA-1?, 3, 6, 9, 12 Py	Diagenetic-F
BAB1	2940	Government	Coronation	942	QTZ	0.16	−38.1				SO	Drill	2.5	−0.6			DIA-6 Py	Diagenetic-F
											SF6	Drill	2.4	−0.6	−0.3	940	DIA-6 Py	Diagenetic-F
BAB1	2940	Government	Coronation	947	D	0.02	−34.7		0.19	9.7	SO	Bulk	3.0	0.0			DET-1, 2 Py. DIA-2, 6, 9 Py. EPI-1, 4 Py	MIX
BAB1	2940	Government	Coronation	954	D						SO	Drill	1.6	0.0			DET-2 Cpy (with Aln)	DET
				954	CM						SF6	Drill	3.2	−0.5	−0.4	3457	DIA-1, 2, 3, 6, 9, 12 Py	Diagenetic-F
BAB1	2940	Government	Coronation	959	D	0.02	−32.5		0.16	9.9	SO	Bulk	3.6	0.3			DET-1, 2. DIA-2, 6 Py. DIA-6/EPI-1 Py	MIX
											SO	Drill	7.7	0.1			DET-2 Py (euhedral crystals in chert clast)	DET
BAB1	2940	Government	Coronation	979	D	0.02	−33.9		0.24	11.5	SO	Bulk	4.4	0.5			DET-1, 2 Py. DIA-3, 6 Py	MIX
											SO	Drill	−1.4	0.3			DET-2 Py (disseminated layer in chert clast)	DET
BAB1	2940	Government	Coronation	987	D	0.03	−35.0		0.26	9.7	SO	Bulk	4.1	0.3			DET-1, 2 Py. DIA-3, 6, 9 Py. EPI-4 Py	MIX
BAB1	2940	Government	Coronation	993	CM				0.22		SF6	Drill	4.7	−1.4	−0.1	2416	DIA-5 Py	Diagenetic-F
											SO	Bulk	5.5	0.1			DIA-2, 3, 5, 6, 9, 12 Py. EPI-3 Py	Diagenetic-F
BAB1	2940	Government	Coronation	994	W	0.09	−39.4		0.26	3.0	SO	Bulk	4.1	0.1			DET-1, 2 Py. DIA-3, 5, 6, 9, 12 Py. EPI-3 Py	MIX
BAB1	2940	Government	Coronation	1000	U.D	0.03	−34.4		0.17	6.7								
				1000	CM	0.09	−38.1		0.17	2.0	SO	Drill	13.0	1.3		2022	DIA-3 Py	Diagenetic-F
											SF6	Drill	16.5	1.2	−2.9	2022	DIA-3 Py	Diagenetic-F
				1000	L.D	0.02	−33.7		0.17	8.9								
BAB1	2940	Government	Coronation	1010	QTZ-W	0.04	−35.3		0.18	4.4								
BAB1	2940	Government	Coronation	1012	D	0.03	−37.5		0.25	8.9								
BAB1	2940	Government	Coronation	1013	ICM	0.22	−44.3		1.06	4.9	SO	Bulk	0.4	0.3			DIA-2	Diagenetic-F
											SO	Drill	1.0	0.5			DIA-2	Diagenetic-F
											SF6	Drill	0.9	0.0	−0.7	7149	DIA-2	Diagenetic-F

BAB1	2940	Government	Coronation	1015	QTZ-SI	*0.09*	*−38.1*	0.17	1.9	SO	Bulk	4.8	0.1			DET-1, 2 Py. DIA-2, 3, 6, 9, 12 Py	MIX
BAB1	2940	Government	Coronation	1016	QTZ	0.01	−29.8										
BAB1	2940	Government	Coronation	1030	QTZ-SI			0.19		SF6	Drill	3.9	−1.2	−0.2	2054	DIA-2 Py	Diagenetic-F
										SO	Bulk	5.5	0.2			DET-2 Py. DIA-2, 3, 6, 9, 12 Py	MIX
BAB1	2940	Government	Promise	1066	QTZ-SI	*0.07*	*−37.5*	0.07	1.1	SF6	Drill	11.4	−1.1	−1.3	2294	DIA-2 Py (sandstone)	Diagenetic-F
BAB1	2940	Government	Promise	1079	ICM			0.27		SO	Drill	1.2	0.0			EPI-1 Py (porous)	EPI
BAB1	2940	Government	Promise	1082	W	*0.10*	*−39.6*	0.48	4.8	SF6	Drill	7.5	−1.2	−0.6		DIA-2 Py	Diagenetic-F
										SF6	Drill	6.6	−0.7	−0.8		DIA-2 Py (CuS, PbS cores)	Diagenetic-F
										SF6	Drill	3.1	−0.3	−0.4		DIA-2 Py (coalesced into DIA-5)	Diagenetic-F
										SO	Bulk	4.2	0.3			DIA-2, 5, 6, 9 Py	Diagenetic-F
BAB1	2940	Government	Promise	1120	QTZ-SI	*0.10*	*−39.7*	0.14	1.5	SO	Bulk	2.8	0.1			DIA-2, 3, 6, 9, 12 Py	Diagenetic-F
BAB1	2940	Government	Promise	1138	ICM	*0.14*	*−41.5*	1.29	9.2	SF6	Drill	7.7	−0.6	−0.8		DIA-2 Py (sandstone intercalation)	Diagenetic-F
										SF6	Drill	3.3	−0.4	−0.2	2580	DIA-4 Py	Diagenetic-F
										SO	Bulk	3.1	−0.1		2580	DIA-1, 2, 3, 4, 6, 9, 12 Py. EPI-1, 3 Py	Diagenetic-F
BAB1	2940	Government	Promise	1151	ICM	*0.10*	*−44.0*	0.41	4.2	SF6	Drill	3.3	−0.3	−0.6		DIA-5 Py (sandstone intercalation)	Diagenetic-F
										SO	Bulk	3.2	0.0			DIA-2, 3, 5, 6, 9, 12 Py. EPI-1 Py	Diagenetic-F
BAB1	2940	Government	Promise	1155	ICM	*0.09*	*−42.3*	1.07	11.7	SF6	Drill	0.6	−0.1	−0.7	3225	DIA-4 Py	Diagenetic-F
										SF6	Drill	3.7	0.2	−1.8	2386	DIA-2 Py (sandstone intercalation)	Diagenetic-F
										SO	Bulk	2.2	0.3			DET-1, 2 Py. DIA-2, 3, 4, 6, 9, 12 Py. EPI-1 Py	MIX
BAB1	2940	Government	Promise	1157	ICM	0.10	−39.5	0.75	7.7	SO	Bulk	1.3	0.2			DIA-2, 3, 6 Py. EPI-1, 2, 3 Py	MIX
										SF6	Drill	1.6	−0.3	−0.6	2058	DIA-2 Py	Diagenetic-F
BAB1	2940	Government	Promise	1157	ICM	*0.08*	*−39.8*	0.22	2.6	SF6	Drill	2.1	−0.2	−0.4		DIA-2 Py (coalesced into DIA-5)	Diagenetic-F
										SO	Bulk	2.4	0.0			DET-1 Py. DIA-2, 3, 5, 6, 9,12 Py. EPI-3 Py	Diagenetic-F
BAB1	2940	Government	Promise	1172	ICM	0.10	−40.8	0.15	1.5	SO	Bulk	3.3	0.1			DIA-3, 6, 9, 12 Py	Diagenetic-F
BAB1	2940	Government	Promise	1211	ICM	0.05	−39.3	0.43	8.5	SO	Bulk	4.5	0.2			DET-1 Py. DIA-1, 2, 3, 6, 9 Py. EPI-5 Po	MIX
BAB1	2940	Government	Promise	1220	ICM	0.05	−38.3	0.49	9.4	SO	Bulk	3.2	0.4			*DIA-3, 9, 12 Po. EPI-3, 5 Po	MIX
BAB1	2940	Government	Promise	1224	ICM	0.05	−37.2	0.51	9.4	SO	Bulk	2.8	0.3			*DET-1 Po. *DIA-3, 6 Po. EPI-4, 5 Po	MIX
										SO	Drill	2.9	0.3		2777	DIA-5 Py	Diagenetic-F
BAB1	2940	Government	Promise	1230	D	0.03	−35.9	0.24	7.1	SO	Bulk	3.3	0.2			EPI-4 Po (quartz). EPI-5 Po	EPI
BAB1	2941	Government	Promise	1231	ICM			0.22		SF6	Bulk	3.0	0.1	−1.0		*DET-1 Po? *DIA-2, 6 Po. EPI-4 (quartz). EPI-5 Po	MIX
BAB1	2940	Government	Promise	1236	ICM	0.06	−38.2	0.39	6.4	SO	Bulk	4.6	0.0			*DIA-2, 6 Po. EPI-5 Po	MIX
										SO	Drill	3.1	0.4			*DIA-2, 5 Po/EPI-4 Po	AMB
BAB1	2940	Government	Promise	1246	ICM	0.05	−36.9	0.33	7.2	SO	Bulk	3.9	−0.4			*DIA-3 Po. EPI-5 Po	EPI
BAB1	2940	Government	Promise	1251	ICM	*0.03*	*−36.0*	0.01	0.2								
BAB1	2940	Government	Promise	1262	ICM-Red	*0.01*	*−25.2*	3.52	428.0	SO	Bulk	2.8	0.2			EPI-4, 5 Po	EPI
BAB1	2940	Government	Promise	1263	ICM	*0.01*	*−25.2*	0.98	120.7	SO	Bulk	2.2	−0.1			EPI-4, 5 Po	EPI
										SO	Drill	1.3	0.6			*DIA-5 Po/EPI-4, 5 Po	AMB
										SO	Drill	1.2	0.3			*DIA-5 Po/EPI-4, 5 Po	AMB
BAB1	2940	Government	Promise	1303	ICM	*0.00*	*−25.0*	0.18	43.5	SO	Bulk	2.5	−0.3			EPI-5 Po	EPI
BAB1	2940	Government	Promise	1313	ICM	*0.01*	*−26.3*	0.09	16.1	SO	Bulk	3.4	−0.4			EPI-5 Po	EPI
BAB1	2940	Government	Eleazar	1348	ICM	0.05	−36.8	0.15	2.8	SO	Bulk	5.1	0.0			*DET-1 Po. *DIA-3, 9, 12 Po. EPI-5 Po	MIX
BAB1	2940	Government	Eleazar	1356	ICM	0.04	−28.4	0.23	5.9	SO	Bulk	2.8	0.3			DIA-5 Py. EPI-5 Po	MIX
TF1	2960	Hospital Hill	Brixton	3015	NM	*0.02*	*−26.3*	0.03	1.6								
TF1	2960	Hospital Hill	Brixton	3035	ICM	0.12	−26.1	0.13	1.1	SO	Bulk	1.9	0.6			*DIA-3 Po. EPI-4 Po (quartz)	MIX
TF1	2960	Hospital Hill	Brixton	3055	ICM	0.10	−28.0	0.01	0.1								
TF1	2960	Hospital Hill	Brixton	3070	ICM	*0.06*	*−24.6*	0.01	0.1	SO	Drill	4.3	1.0		807	DIA-5 Py	Diagenetic-PM
										SF6	Drill	4.4	1.0	−1.6	807	DIA-5 Py	Diagenetic-PM
TF1	2960	Hospital Hill	Brixton	3080	INM	*0.01*	*−23.7*	0.01	0.9								
TF1	2960	Hospital Hill	Brixton	3090	NM	*0.03*	*−24.4*	0.01	0.3								
TF1	2960	Hospital Hill	Brixton	3105	MM	0.02	−24.9	0.00	0.2								

Table 2 (*Continued*)

Core	Age (Ma)	Subgroup	Formation	Depth (m)	Lithology	C_{org} (wt.%)	$\delta^{13}C_{org}$ (‰)	$\delta^{13}C_{carb}$ (‰)	S (wt.%)	S/C	Analysis	Method	$\delta^{34}S$ (‰)	$\Delta^{33}S$ (‰)	$\Delta^{36}S$ (‰)	Ni_{py} (ppm)	Textural descriptions	Association
TF1	2960	Hospital Hill	Brixton	3111	IMM	0.02	−22.4		0.06	2.9	SO	Bulk	2.7	0.1			DIA-6 Py (rare)	Diagenetic-DM
TF1	2960	Hospital Hill	Parktown	3500	ICM				0.11									
TF1	2960	Hospital Hill	Parktown	3515	ICM	0.08	−26.9				SO	Bulk	5.5	0.2			*DET-1 Po. EPI-5 Po	MIX
TF1	2960	Hospital Hill	Parktown	3570	ICM	0.09	−27.4		0.12	1.4	SO	Bulk	5.5	0.4			EPI-5 Po	EPI
TF1	2960	Hospital Hill	Parktown	3610	ICM	0.11	−27.9		0.13	1.2	SO	Bulk	5.2	0.5			EPI-5 Po	EPI
TF1	2960	Hospital Hill	Parktown	3670	ICM	0.20	−27.7		0.11	0.6	SO	Bulk	5.4	0.1			EPI-3 Po. EPI-5 Po	EPI
TF1	2960	Hospital Hill	Parktown	3710	ICM	0.16	−27.1		0.10	0.6	SO	Bulk	5.6	0.0			EPI-5 Po	EPI
TF1	2960	Hospital Hill	Parktown	3730	W						SO	Drill	4.8	0.5			EPI-1 Py	EPI
TF1	2960	Hospital Hill	Parktown	3760	NM	*0.01*	*−26.6*		0.04	2.6								
TF1	2960	Hospital Hill	Parktown	3775	Sid-IF	*0.01*	*−24.2*		0.08	8.9	SO	Bulk	6.5	0.6		241	DIA-5, 6, 11 Py	Diagenetic-DM
											SF6	Bulk	6.3	0.3	−1.8	241	DIA-5, 6, 11 Py	Diagenetic-DM
TF1	2960	Hospital Hill	Parktown	3783	BIF	*0.01*	*−21.9*		0.00	0.3								
TF1	2960	Hospital Hill	Parktown	3784	Py-NM	*0.01*	*−26.8*		0.37	31.7	SO	Bulk	1.1	0.6		146	DET-2/DIA-12 Py. DIA-5, 6 Py	Diagenetic-DM
											SF6	Bulk	1.2	0.2	−0.9	146	DET-2/DIA-12 Py. DIA-5, 6 Py	Diagenetic-DM
TF1	2960	Hospital Hill	Parktown	3790	Ank-NM	0.02	−25.6		0.12	6.2	SO	Bulk	5.5	1.2			DIA-5 Po, Cob, Cpy. DIA-6 Py	Diagenetic-DM
											SO	Drill	3.8	1.1			DIA-5 Po, Cob, Cpy	Diagenetic-DM
											SF6	Bulk	4.9	0.9	−1.4		DIA-5 Po, Cob, Cpy. DIA-6 Py	Diagenetic-DM
TF1	2960	Hospital Hill	Parktown	3795	MM	*0.01*	*−24.9*		0.01	0.8								
TF1	2960	Hospital Hill	Parktown	3800	MM	*0.01*	*−25.2*		0.00	0.5								
TF1	2960	Hospital Hill	Parktown	3804	IMM	*0.01*	*−25.9*		0.01	0.6								
TF1	2960	Hospital Hill	Parktown	3805	MM						SO	Drill	3.6	0.6			EPI-3 Py	EPI
TF1	2960	Hospital Hill	Parktown	3810	MM	*0.01*	*−25.6*		0.01	1.1								
TF1	2960	Hospital Hill	Parktown	3815	IMM	0.01	−25.5		0.02	1.7								
TF1	2960	Hospital Hill	Parktown	4315	INM	*0.03*	*−29.3*		0.00	0.1								
TF1	2960	Hospital Hill	Parktown	4326	MM	0.02	−26.1	−15.5	0.04	2.1	SO	Bulk	1.8	0.0			Could not detect sulfides	AMB
TF1	2960	Hospital Hill	Parktown	4330	QTZ						SO	Drill	0.6	0.1			DIA-6/EPI-1 Py	AMB
TF1	2960	Hospital Hill	Parktown	4333	BIF	0.02	−24.0	−13.0	0.01	0.3								
TF1	2960	Hospital Hill	Parktown	4335	BIF						SO	Drill	2.9	1.3		178	DIA-6 Py (Incl.-free)	Diagenetic-DM
											SF6	Drill	3.2	1.2	−2.2	178	DIA-6 Py (Incl.-free)	Diagenetic-DM
TF1	2960	Hospital Hill	Parktown	4340	MM/BIF	0.01	−23.0	−13.0	0.06	4.6	SO	Bulk	3.0	1.9		238	DIA-6 Py	Diagenetic-DM
											SO	Drill	3.3	1.7		238	DIA-6 Py (Mt inclusions)	Diagenetic-DM
											SF6	Drill	3.2	1.4	−2.2	238	DIA-6 Py (Mt inclusions)	Diagenetic-DM
TF1	2960	Hospital Hill	Parktown	4350	MM	*0.02*	*−23.2*	−13.3	0.01	0.7								
TF1	2960	Hospital Hill	Parktown	4355	MM						SO	Drill	2.1	1.5		147	DIA-7 Py	Diagenetic-DM
											SF6	Drill	2.8	1.1	−1.8	147	DIA-7 Py	Diagenetic-DM
TF1	2960	Hospital Hill	Parktown	4360	MM	*0.02*	*−24.5*	−16.5	0.01	0.5								
TF1	2960	Hospital Hill	Parktown	4369	MM						SO	Drill	3.0	1.2		172	DIA-7 Py	Diagenetic-DM
											SF6	Drill	2.3	1.3	−2.0	172	DIA-7 Py	Diagenetic-DM
TF1	2960	Hospital Hill	Parktown	4370	MM	*0.01*	*−23.2*	−16.4	0.01	0.6								
TF1	2960	Hospital Hill	Parktown	4375	MM	0.01	−25.9	−16.5	0.01	0.7								
TF1	2960	Hospital Hill	Parktown	4377	Sid-Ank	0.02	−23.5	−13.9										
TF1	2960	Hospital Hill	Parktown	4380	Sid-Ank	*0.02*	*−23.7*	−14.2	0.01	0.5								
TF1	2960	Hospital Hill	Parktown	4385	CM	0.63	−27.5		0.02	0.0	SO	Drill	5.0	0.3			DIA-7 Py?	AMB
TF1	2960	Hospital Hill	Parktown	4390	CM	0.67	−27.6		0.01	0.0								
TF1	2960	Hospital Hill	Parktown	4395	CM	0.71	−27.6		0.01	0.0								
TF1	2960	Hospital Hill	Parktown	4400	CM	0.88	−27.9		0.03	0.0	SO	Drill	3.0	1.2		843	DIA-7 Py	Diagenetic-PM
TF1	2960	Hospital Hill	Parktown	4405	CM	0.58	−27.7		0.02	0.0	SO	Drill	2.3	0.6		4569	DIA-7 Py	Diagenetic-PM
TF1	2960	Hospital Hill	Parktown	4410	ICM	0.60	−27.5		0.05	0.1	SO	Bulk	2.8	N/A		2001	DIA-6, 7 Py	Diagenetic-PM
TF1	2960	Hospital Hill	Parktown	4415	ICM	0.38	−27.6		0.10	0.3	SO	Bulk	3.1	0.3			*DIA-3 Po? DIA-7 Py? EPI-5 Po	MIX
TF1	2960	Hospital Hill	Parktown	4420	ICM	0.28	−27.0		0.02	0.1								
TF1	2960	Hospital Hill	Parktown	4430	ICM	0.23	−28.1		0.08	0.3	SO	Bulk	5.2	0.0			EPI-5 Po	EPI
TF1	2960	Hospital Hill	Parktown	4440	ICM	0.29	−27.4		0.02	0.1								
TF1	2960	Hospital Hill	Parktown	4455	ICM	0.22	−27.5		0.04	0.2								

Lithology: I: intercalated siltstone/sandstone; NM: non-magnetic shale/mudstone; CM: carbonaceous shale/mudstone; MM: magnetic shale/mudstone; LAVA: lava; IF: iron formation; BIF: banded iron formation; D: diamictite; SI: shale interbeds; W: wackestone; QTZ: sandstone; Sid: siderite-bearing; Ank: ankerite-bearing; U/L: upper/lower.

Mineralogy: Aln: allanite; Mt: magnetite; Py: pyrite/pyritic; Po: pyrrhotite; Cpy: chalcopyrite; Cob: cobaltite; Agg's: aggregates; Incl.: inclusion; *: pyrrhotite pseudomorph.

Depofacies and paragenetic associations: Diagenetic-PM: diagenetic pyrite-proximal marine; Diagenetic-DM: diagenetic pyrite-distal marine; Diagenetic-F: diagenetic pyrite-fluvial-dominated; DET: detrital pyrite; EPI: epigenetic pyrite; MIX: paragenetic pyrite mixtures; AMB: pyrite of ambiguous origin.

Other: N/A: not reported due to large error/low bulk rock S content; Italic C_{org} data: Carbon analysis performed in single (duplicate otherwise); DIA-**6** Py: Bold indicates pyrite type for Ni content (Guy et al., 2010).

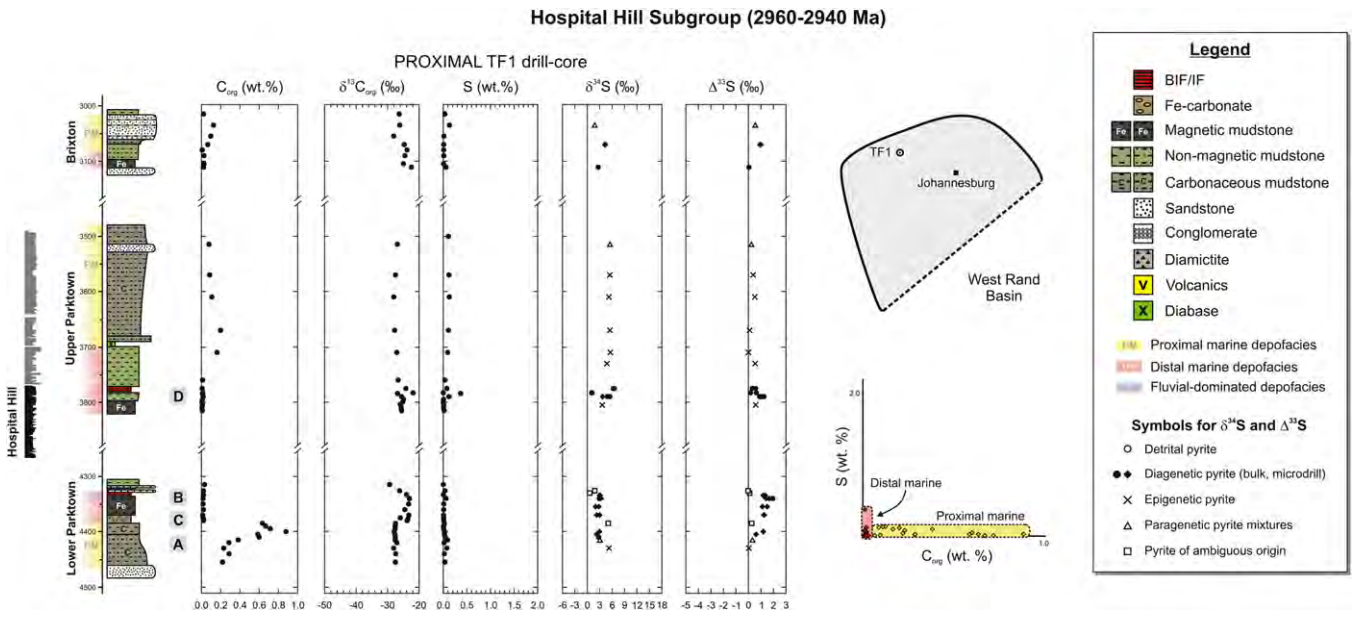

Fig. 6. Sampled intersections and geographic position of the proximal TF1 drill-core in the West Rand Basin. S/C plot illustrates proximal and distal marine depofacies. (A) Carbonaceous mudstone of the proximal marine depofacies (low sulfur, high carbon and $\delta^{13}C_{org}$ ~−28‰). (B) Magnetic mudstone and BIF of the distal marine depofacies (low sulfur, low carbon, high $\delta^{13}C_{org}$ and positive $\Delta^{33}S$). (C) Fe-carbonate concretions. (D) Pyrite-bearing non-magnetic mudstone underlying Contorted Bed BIF.

carbon) and proximal marine depofacies (low sulfur contents and positive $\Delta^{33}S$) (Fig. 8E).

5.4. Sulfur addition (high S, low C)

This group is composed of samples that possess an abundance of detrital pyrite or epigenetic pyrite/pyrrhotite (Figs. 5D, 7G, 8C and Table 2). With reference to the former, the pyrite in four diamictite clasts (DET-2) from the Kensington and Lagerspoort members display near-zero $\Delta^{33}S$ values (0.0 to +0.3‰), whereas $\delta^{34}S$ values range from −1.4 to +7.7‰ (Table 2). Regarding the latter, pyrrhotite-rich samples near a diabase sill in the Promise Formation display high S/C ratios (~428), high sulfur contents (~3.5 wt.%), low organic carbon contents (~0.01 wt.%) and high $\delta^{13}C_{org}$ values (~−25‰) (see alteration halo in Fig. 7G). $\delta^{34}S$ and $\Delta^{33}S$ values average +2.3 and +0.1‰, respectively. A highly faulted and pyritic mudstone in the Rietkuil Formation yields a similar set of geochemical characteristics (Table 2). In the upper Parktown Formation, disseminated crystals of epigenetic pyrrhotite in siltstone and sandstone laminae near a diabase sill exhibit uniform sulfur isotope signatures ($\delta^{34}S$ and $\Delta^{33}S$ values average ~+5.3 and +0.3‰, respectively) (Fig. 6).

6. Multiple sulfur and organic carbon isotopes in a depofacies context

6.1. Proximal marine depofacies

The scarcity of early diagenetic pyrite in shallow marine carbonaceous mudstone from the Hospital Hill Subgroup is reflected by extremely low bulk rock S/C ratios around 0.03 (Figs. 5A and 6A). In modern sediments, such low S/C ratios are characteristic of sulfate-poor fresh water environments (e.g., Berner and Raiswell, 1984; Watanabe et al., 1997). However, a number of sedimentological features suggest a marine setting for the Hospital Hill Subgroup, including polymodal and bimodal-bipolar paleocurrent directions, supermature quartz arenites, extensive shale deposits and banded iron formation (Camden-Smith, 1980; Eriksson et al., 1981; Beukes and Cairncross, 1991; Beukes, 1995; Beukes and Nelson, 1995; Coward et al., 1995; Frimmel et al., 2005). This implies either that mesophilic microbial sulfate reduction had not developed by ~2.96 Ga, the electron donor (i.e., the organic matter) was unsuitable for microbial sulfate reduction, or that the Archean ocean was sulfate-limited (Habicht et al., 2002). The latter option is preferred since an early Archean origin (3.5 Ga) for microbial sulfate reduction has been suggested (Shen et al., 2001; Ueno et al., 2008). The relatively high organic carbon content, coupled with $\delta^{13}C_{org}$ values around ~−28‰, is consistent with primary contributions from oxygenic or anoxygenic photosynthetic microorganisms in a shallow marine environment (Fig. 9A) (Brocks et al., 1999; Des Marais, 2000; Eigenbrode and Freeman, 2006; Noffke et al., 2006, 2008; Ono et al., 2006a; Tice and Lowe, 2006a; Buick, 2008). The positive $\Delta^{33}S$ values measured from rare diagenetic pyrite suggest inputs from insoluble polymerized elemental sulfur aerosols (S_8) (Fig. 9B) (Farquhar et al., 2000; Ono et al., 2003).

6.2. Distal marine depofacies

6.2.1. Hospital Hill Subgroup

The low sulfur content in Fe-rich rocks from the Hospital Hill Subgroup (~0.02 wt.%, Fig. 5B) is consistent with a ferruginous and sulfate-poor water column in the distal marine shelf environment. However, a transient rise in sulfur concentrations prior to BIF deposition (up to 0.4 wt.%) may signal titration of reduced sulfur by upwelling ferrous seawater (Fig. 6D). Compared to the proximal marine depofacies, organic carbon contents are significantly lower (0.01 wt.%) and $\delta^{13}C_{org}$ values are high (~−26 to −22‰) (Fig. 9A). The source of the original biomass may have been derived endogenetically via photoautotrophic and/or chemolithoautotrophic iron-oxidizing bacteria (Kappler et al., 2005; Beukes and Gutzmer, 2008). Alternatively, it may have been transported from areas of high primary productivity, which would have resulted in the sparse deposition of ^{13}C-enriched organic matter due to slow depositional rates, longer transport distances and effective biological degradation (Hayes, 1983; Beukes et al., 1990; Tice and Lowe, 2006b). In sub-surface diagenetic environments, the presence of ^{13}C-depleted Fe-carbonate, with $\delta^{13}C_{carb}$ values down to −16.5‰, suggests that Fe(III)-respiration was an important metabolic pathway for respiring microorganisms (Fig. 6C and Table 2). The majority of diagenetic

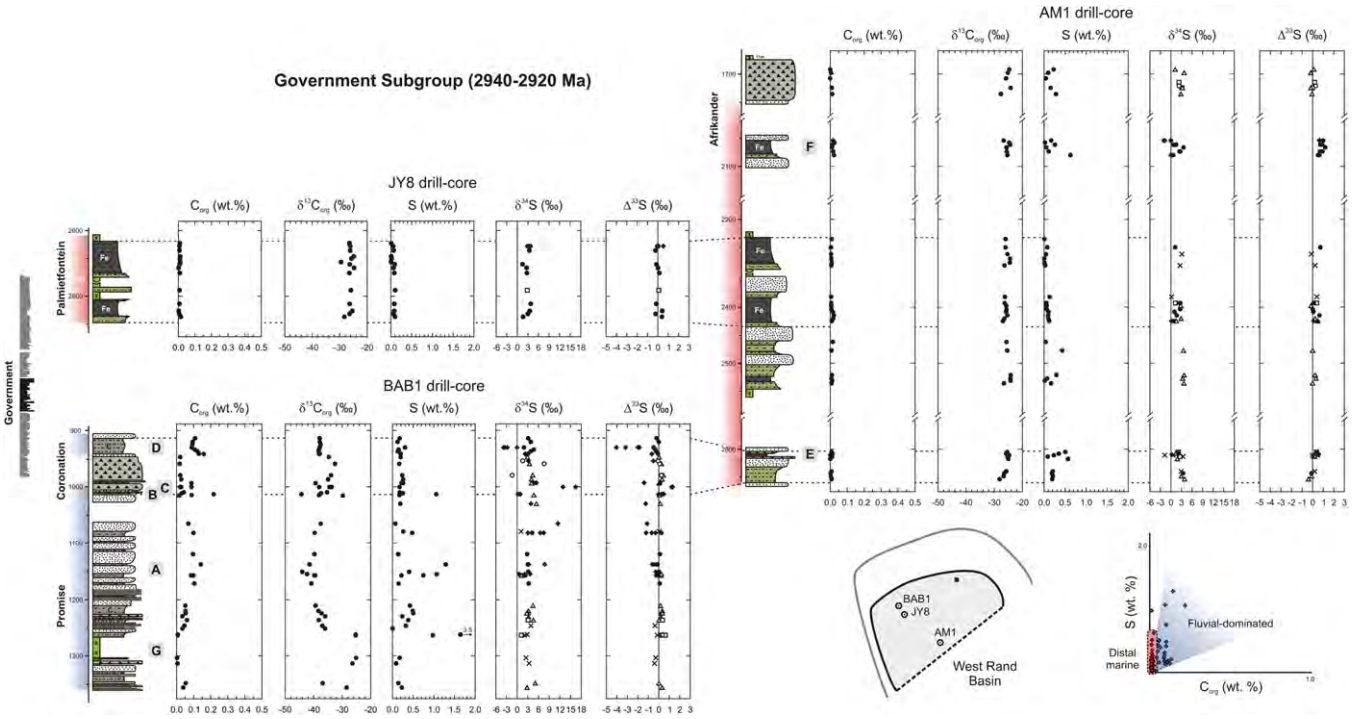

Fig. 7. Sampled intersections and geographic positions of the proximal BAB1, intermediate JY8 and distal AM1 drill-cores in the West Rand Basin. S/C plot illustrates fluvial-dominated and distal marine depofacies. (A) Carbonaceous siltstone-shale of the fluvial-dominated depofacies (high sulfur, high carbon, low $\delta^{13}C_{org}$ and negative $\Delta^{33}S$). (B) Carbonaceous siltstone-shale underlying diamictite (high sulfur, high carbon, low $\delta^{13}C_{org}$ and negligible $\Delta^{33}S$). (C) Carbonaceous shale in diamictite with a high $\delta^{34}S$ value (+16.5‰) and a positive $\Delta^{33}S$ value (+1.2‰) (DIA-3). (D) Pyrite nodules (DIA-5) in carbonaceous shale exhibiting negative $\delta^{34}S$ (−3.7‰) and negative $\Delta^{33}S$ (down to −4.0‰). (E) Finely laminated iron formation from the correlative distal marine depofacies. High sulfur content reflects epigenetic pyrite (EPI-1, 3). (F) Non-magnetic mudstone and magnetic mudstone of the distal marine depofacies (positive $\Delta^{33}S$) (DIA-3, 5). (G) Diabase sill in the Promise Formation. Note geochemical alteration halo.

pyrite in distal Fe-rich settings is characterized by positive $\Delta^{33}S$ values; which implies the same (or a similar) reduced sulfur reservoir as encountered in the proximal marine depofacies (Fig. 9B). The most positive $\Delta^{33}S$ values are recorded during maximum marine transgression, i.e., during deposition of BIF (up to +1.9‰). Ono et al. (2009b) noted that argillites with high iron contents contain pyrite with large positive $\Delta^{33}S$ signatures, and that the presence of iron appears to be critical in terms of S_8 sequestration. Similar relationships are observed for rocks from the Witwatersrand Supergroup, where samples with the highest iron contents (>20 wt.%) and the lowest bulk rock sulfur and organic carbon contents (<0.1 and <0.02 wt.%, respectively) contain the most positive $\Delta^{33}S$ anomalies.

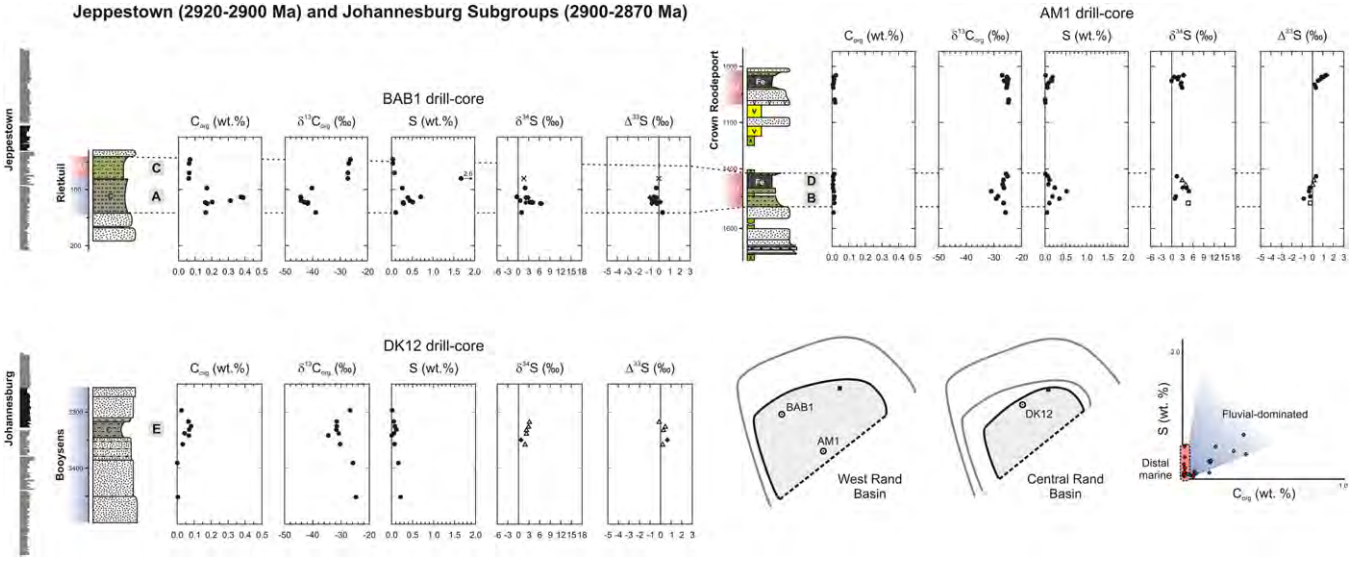

Fig. 8. Sampled intersections and geographic positions of the proximal BAB1, proximal DK12 and distal AM1 drill-cores in the West Rand and Central Rand Basins. S/C plot illustrates fluvial-dominated and distal marine depofacies. (A, B) Lowstand argillite unit of Rietkuil Formation. (A) Carbonaceous siltstone-shale of the fluvial-dominated depofacies (high sulfur, high carbon, low $\delta^{13}C_{org}$ and negative $\Delta^{33}S$). (B) Non-magnetic mudstone of the distal marine depofacies (high sulfur, low carbon, slightly depleted in $^{13}C_{org}$ and negative $\Delta^{33}S$). (C, D) Highstand argillite unit of Rietkuil Formation. (C) Non-magnetic mudstone and (D) magnetic mudstone of the distal marine depofacies (low sulfur, low carbon, high $\delta^{13}C_{org}$ and positive $\Delta^{33}S$). (E) Transitional depofacies of the Booysens Formation (fluvial-dominated and marine depofacies).

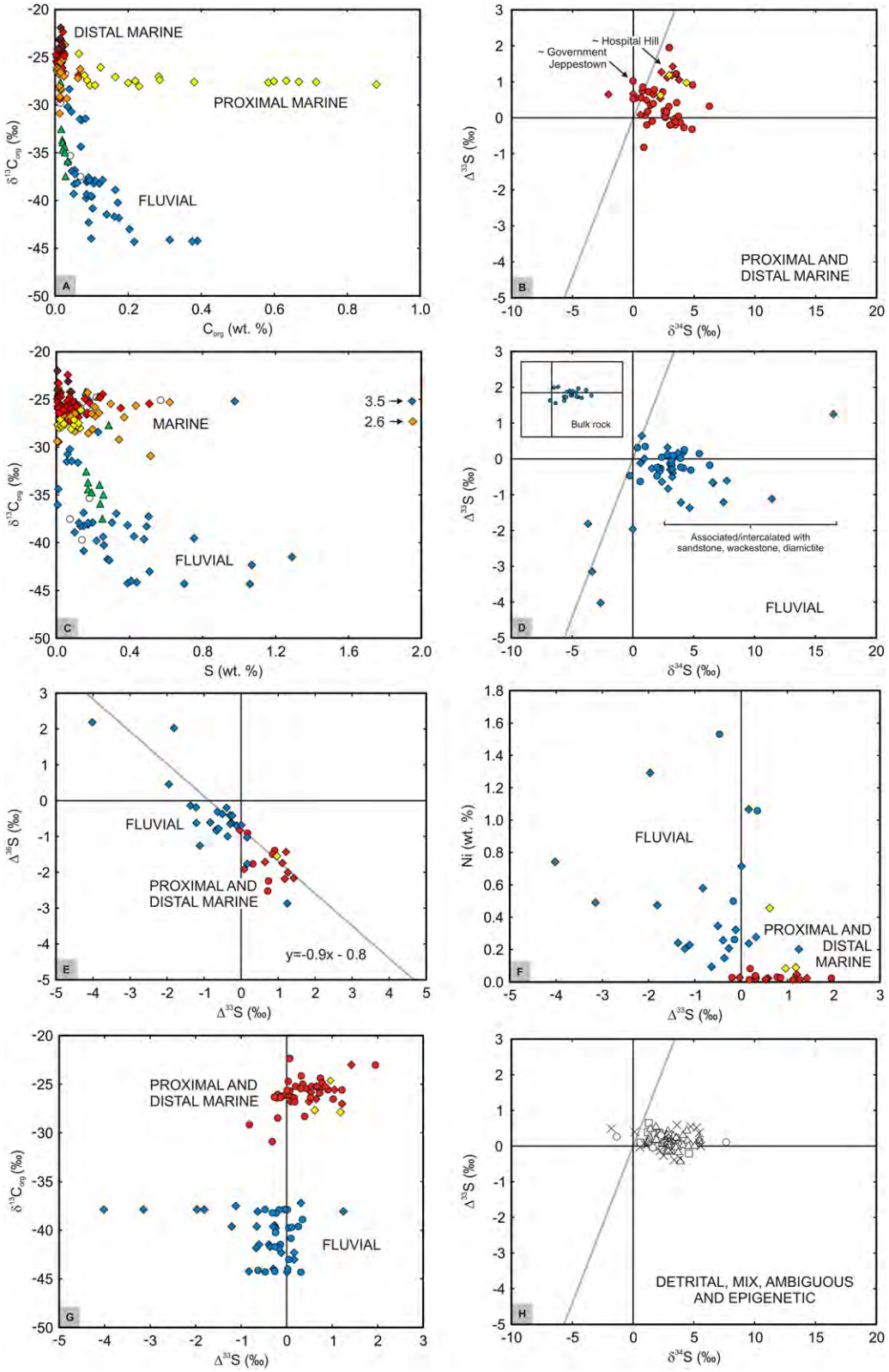

Fig. 9. Sulfur and organic carbon plots. (A) $\delta^{13}C_{org}$ versus C_{org} wt.%. (B) $\Delta^{33}S$ versus $\delta^{34}S$ for diagenetic pyrite in proximal and distal marine depofacies. (C) $\delta^{13}C_{org}$ versus S wt.%. (D) $\Delta^{33}S$ versus $\delta^{34}S$ for diagenetic pyrite in fluvial-dominated depofacies. Inset displays bulk rock samples. (E) $\Delta^{36}S$ versus $\Delta^{33}S$ for diagenetic pyrite in marine and fluvial-dominated depofacies. The $\Delta^{36}S/\Delta^{33}S$ slope of −0.9 is consistent with SO_2 photolysis (Farquhar et al., 2001; Kaufman et al., 2007; Ono et al., 2009a). (F) Ni_{py} versus $\Delta^{33}S$ for diagenetic pyrite in marine and fluvial-dominated depofacies. Ni data from Guy et al. (2010). (G) $\delta^{13}C_{org}$ versus $\Delta^{33}S$ for diagenetic pyrite in marine and fluvial-dominated depofacies. (H) $\Delta^{33}S$ versus $\delta^{34}S$ for non-diagenetic pyrite (i.e., detrital pyrite, paragenetic pyrite mixtures from bulk rock analyses, ambiguous pyrite and epigenetic pyrite). Overlapping isotopic ranges for diagenetic and epigenetic pyrite indicate a relatively closed sulfur system during post-depositional alteration. For plots (A) and (C) refer to Fig. 5 for symbols. For plots (B), (D), (E), (F), (G) and (H) refer to Fig. 6 for symbols. For plots (B), (D) and (H), line is Archean Reference Array ($\Delta^{33}S = 0.89\ \delta^{34}S$). Data from the SO method was omitted when samples contained both SO and SF_6 data. On average, $\Delta^{33}S$ data from the SO method were ~+0.2‰ greater than $\Delta^{33}S$ data from the SF_6 method.

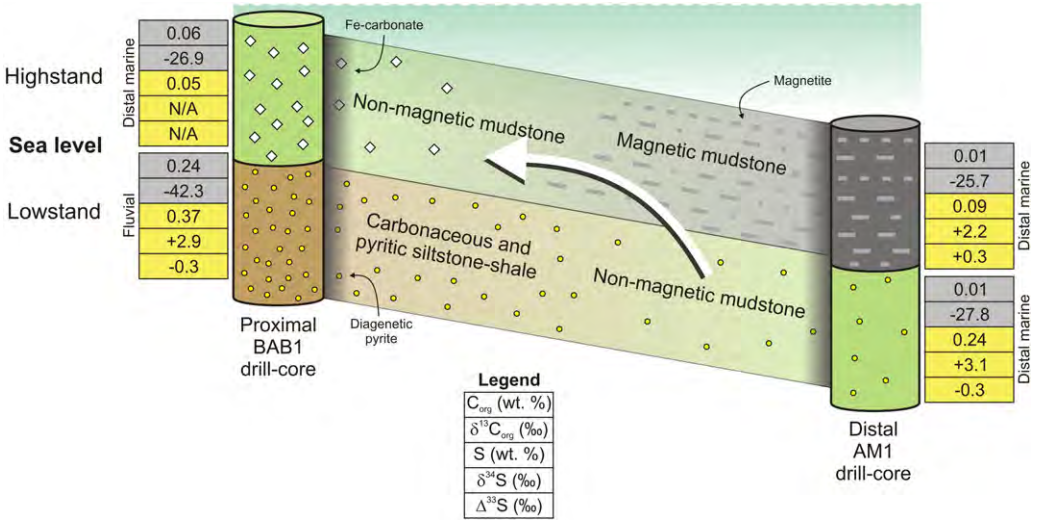

Fig. 10. Schematic illustration of the Rietkuil Formation in the proximal BAB1 and distal AM1 drill-cores. Arrow illustrates the concept that a conformable vertical succession of sedimentary facies reflects their former lateral juxtaposition (Walther, 1894). N/A: sulfur contents too low for sulfur isotope analyses.

Furthermore, these Fe-rich samples lie close to the Archean Reference Array (ARA), which indicates that $\Delta^{33}S$ sequestration proceeded without the involvement of secondary processes (Ono et al., 2003, 2009a; Johnston, 2011). However, a number of samples plot off the ARA and together, display a negative correlation between $\delta^{34}S$ and $\Delta^{33}S$ (Fig. 9B). This most probably suggests mixing with a mass-dependent sulfur reservoir as discussed later in more detail.

6.2.2. Government and Jeppestown subgroups

The majority of diagenetic pyrite from distal marine non-magnetic mudstone, magnetic mudstone and iron formation of the Government and Jeppestown subgroups exhibits positive $\Delta^{33}S$ values. It is worth noting that $\Delta^{33}S$ values are significantly more attenuated in comparison to samples from the Hospital Hill Subgroup (<+1‰) and that most samples fall along a different $\Delta^{33}S$–$\delta^{34}S$ array (Fig. 9B). Not all samples exhibit positive $\Delta^{33}S$ values, however, as negative $\Delta^{33}S$ values were recorded from non-magnetic mudstone from the distal facies of the Coronation and Rietkuil formations. Taken together with the high sulfur contents and relatively ^{13}C-depleted $\delta^{13}C_{org}$ values, these geochemical attributes may signal distal extensions of the fluvial-dominated depofacies (Figs. 8A, B and 10). In both instances, however, positive $\Delta^{33}S$ values return during maximum marine transgression and iron deposition, supporting the link between iron-rich rocks and S_8 sequestration (Figs. 7E, 8C, D and 10) (Ono et al., 2009a,b). The absence of Fe-carbonate in the distal facies of the Rietkuil Formation suggests that organic carbon supplies were too low to sustain dissimilatory Fe-reduction in deeper water settings (Fig. 10) (Beukes and Klein, 1992; Bekker and Kaufman, 2007). Therefore, the presence of magnetite in these distal sediments suggests that the conversion of Fe-oxyhydroxide to magnetite is independent of organic carbon, and may have resulted from the addition of ferrous iron during diagenesis (Ohmoto, 2003).

6.3. Fluvial-dominated depofacies

In contrast to the proximal and distal marine depofacies, samples from the fluvial-dominated depofacies display covariation between sulfur and organic carbon contents (Fig. 5C). The correlation between these two constituents in modern depositional environments has been attributed to the activity of microbial sulfate reducers (e.g., Berner and Raiswell, 1983; Raiswell and Berner, 1986; Kasting et al., 1992), suggesting that microbial sulfate reduction was an important part of the ecological landscape in Mesoarchean times. The antiquity of microbial sulfate reduction is supported by the multiple sulfur isotope compositions of early diagenetic pyrite, e.g., negative $\Delta^{33}S$ values and offsets in $\Delta^{36}S$ (Fig. 9D and E). Negative $\Delta^{33}S$ values have been documented from Archean sulfate deposits (Bao et al., 2007; Ueno et al., 2008) and were likely to have originated from soluble sulfuric acid aerosols derived from the hydrolysis of photolytic SO_2 (Farquhar et al., 2000; Farquhar and Wing, 2003; Ono et al., 2003; Ueno et al., 2009). Offsets in $\Delta^{36}S$ (deviation from $\Delta^{36}S = -0.9\ \Delta^{33}S$) have previously been ascribed to mass-dependent processes, such as microbial sulfate reduction (Ono et al., 2006b; Ueno et al., 2008). The correlation between isotopically light carbon (Fig. 9A) and high bulk rock sulfur contents (or early diagenetic pyrite) (Fig. 9C) implies that microbial sulfate reduction was coupled to the anaerobic oxidation of methane (AOM) (Hinrichs et al., 1999; Hinrichs, 2002; Boetius et al., 2000; Konhauser, 2007). Thus, the highly ^{13}C-depleted $\delta^{13}C_{org}$ values of organic matter in the fluvial-dominated depofacies may signify autotrophic carbon assimilation by a diverse group of organisms, including photoautotrophs, methanogens, anaerobic methanotrophs and sulfate reducers (Schidlowski et al., 1983; Hayes, 1983, 1994; Des Marais, 2001; Eigenbrode and Freeman, 2006; Eigenbrode et al., 2008). Hayes (1994) interpreted the exceptionally ^{13}C-depleted organic carbon (<−60‰) from the ~2.7 Ga Tumbiana Formation as evidence for aerobic methanotrophic microbes. However, free oxygen may not be required to explain the presence of ^{13}C-depleted $\delta^{13}C_{org}$ signatures in the Witwatersrand Supergroup (e.g., Hinrichs, 2002; Thomazo et al., 2009).

Although the majority of pyrite in the fluvial-dominated depofacies is composed of negative $\Delta^{33}S$ values, near-zero and positive $\Delta^{33}S$ anomalies are recorded from bulk rock samples in the proximal facies of the Promise and Coronation formations (Fig. 7C). By comparing micro-drilled and bulk rock sulfur isotope compositions, it is apparent that the near-zero to positive $\Delta^{33}S$ anomalies are hosted by finely disseminated pyrite (DIA-3). Similar observations have been noted from previous studies, where finely disseminated pyrite revealed positive $\Delta^{33}S$ signatures and nodular pyrite revealed negative $\Delta^{33}S$ values (Kamber and Whitehouse, 2007; Ono et al., 2003, 2009b). This small-scale isotope heterogeneity suggests multistage sequestration of sulfur from both oxidized (SO_4) and reduced (S^0) sulfur reservoirs (Ono et al., 2009a).

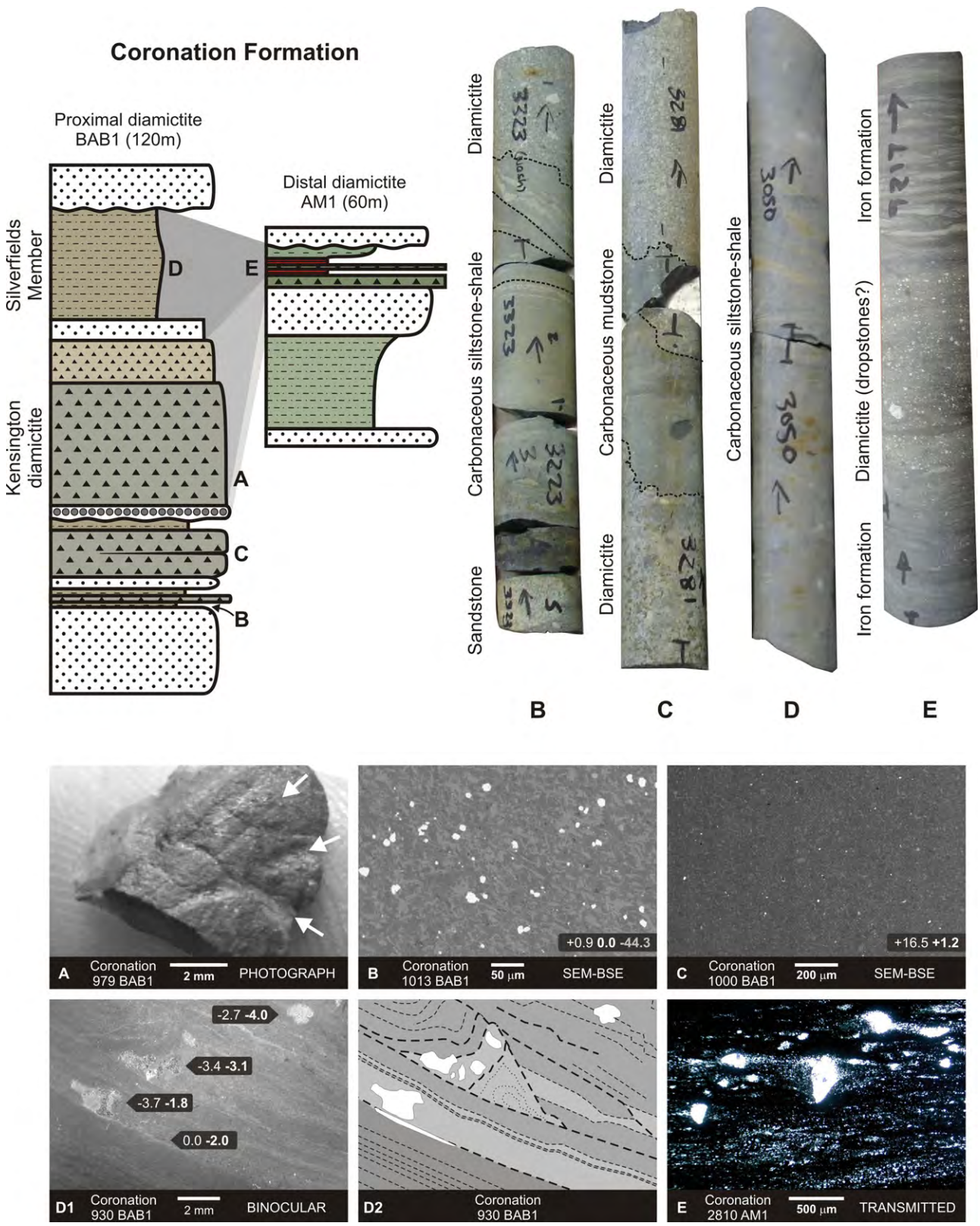

Fig. 11. The Coronation Formation (Kensington diamictite Member). Proximal diamictite (BAB1 drill-core): (A) Possible striations on a chert-pyrite clast (see Fig. 4C). (B) Carbonaceous and pyritic siltstone-shale below diamictite. Note sharp contact and deformation of bedding. Similar features occur below the Witfontein diamictite Member in the BAB1 drill-core. (C) Carbonaceous mudstone parting in diamictite. (D1) Pyrite nodules in carbonaceous siltstone-shale overlying diamictite. Note increase in $\delta^{34}S$ values and decrease in $\Delta^{33}S$ values with time. (D2) Illustration of slumping event and syn-depositional nodule fragmentation (sediment movement was from right to left). Distal diamictite (AM1 drill-core): (E) Silverfields iron formation bisected by diamictite hosting anvil-shaped quartz clasts. Data insets: $\delta^{34}S$ (white regular), $\Delta^{33}S$ (white bold) and $\delta^{13}C_{org}$ (grey bold). Drill-core samples are several decimeters in length.

6.3.1. Interbedded diamictite in the fluvial-dominated depofacies

Anomalous sulfur and organic carbon isotopic compositions were observed from sedimentary rocks interbedded with diamictite in the Coronation Formation (Figs. 7B–E and 11). At the base of the formation, highly ^{13}C-depleted organic carbon (−44.3‰) and mass-dependent sulfur (+0.0‰) isotope signatures were measured from a thin pyritic carbonaceous shale bed underlying the first diamictite unit (Fig. 11B). These geochemical parameters may hint at oxidizing conditions associated with methanotrophy at the onset of glaciation. However, significant S-MIF from diagenetic pyrite within the diamictite (−1.4 to +1.2‰) suggests that atmospheric oxygen levels were kept low during glaciation (Figs. 7 and 11C). The occurrence of a high $\delta^{34}S$ value (up to +16.5‰) within the diamictite is puzzling, since it surpasses the $\delta^{34}S$ composition expected for contemporaneous seawater (+10 to +13‰; Bao et al., 2007). Unusually high $\delta^{34}S$ values have also been documented from sedimentary rocks following Neoproterozoic glacial events, and these anomalous values were attributed to efficient removal of pyrite under extremely low seawater sulfate concentrations (Hurtgen et al., 2002, 2005; Shen et al., 2008; Ries et al., 2009). The observation of highly variable and remarkably negative $\Delta^{33}S$ values from pyrite nodules in transgressive shales overlying the diamictite (∼−2, −3 and −4‰) is consistent with extremely low sulfate concentrations in ambient basin water (Figs. 7D and 11D). These highly ^{33}S-depleted sulfides may represent the sulfur isotope composition of sulfuric acid aerosols that were trapped in glacial ice and were subsequently washed out into a sulfate-poor basin during post-glacial stages. This interpretation is based on the lateral correlation between the pyrite nodules in the BAB1 drill-core and granule-sized lonestones/dropstones in the AM1 drill-core (Fig. 11D and E). An alternative explanation for the highly negative $\Delta^{33}S$ values may be linked to increased levels of optical transparency in the Mesoarchean atmosphere during the period of glaciation (e.g., thinner organic haze and lowered ultraviolet shielding capacity) (e.g., Thomazo et al., 2009).

It is unclear what caused the development of the three putative glacial events in the Government Subgroup. It is, however, interesting to note that the lowermost glacial event closely follows the advent of compressional tectonics in the basin (Beukes, 1995; Schmitz et al., 2004). If this collisional event marks a stage of supercontinent amalgamation, then it could have contributed to colder climatic conditions by increasing Earth's albedo (tectonic uplift) and by the drawdown of CO_2, CH_4 and H_2 via increased silicate and sulfide weathering, photosynthesis, methanotrophy, microbial sulfate reduction and pyrite burial (Eyles, 1993; Evans, 2003; Kasting and Ono, 2006; Kasting and Howard, 2006; Reinhard et al., 2009; Williford et al., 2011). Indeed, the confluence of these factors has been proposed as a trigger mechanism for glaciations in the Proterozoic and Phanerozoic Eons (Evans, 2003; Zahnle et al., 2006). Although tempting to ascribe the extreme sulfur isotopic signatures to these global perturbations in the atmosphere and lithosphere, it is at present, more appropriate to suggest a local control over the geochemical parameters until the diamictite is assessed in more detail from other localities.

7. Tectono-sedimentary and depositional models

In summary, it remains to present a conceptual depositional and tectonic model that integrates and explains the observed sulfur and organic carbon isotope record.

7.1. Trailing margin setting of the Hospital Hill Subgroup

At around 2.96 Ga, a protracted marine transgression flooded the central and southeastern parts of the Kaapvaal Craton. The basal strata of the corresponding depositories, the West Rand and Mozaan groups, represent the proximal and distal parts of a trailing margin basin (Figs. 3 and 12A) (Camden-Smith, 1980; Beukes and Cairncross, 1991; Beukes, 1995, 1996; Beukes and Nelson, 1995; Nelson et al., 1995; Nhleko, 2003). General high-stand of sea level conditions and active creation of accommodation space resulted in the vast accumulation of siliciclastic sedimentary rocks over most of the Kaapvaal Craton. The observation of mature quartz arenites, gradational contacts between lithological units and the scarcity of soft-sediment deformation structures implies rather stable tectonic conditions that were characterized by limited sediment input, much reworking and dispersion of sediment into a wide and open shallow marine shelf environment. The shoreline was characterized by clean and well sorted quartz arenite, wavy and lenticular-laminated siltstone-shale and carbonaceous mudstone (Fig. 12A) (Beukes, 1996). The average $\delta^{13}C_{org}$ composition of these argillaceous sedimentary rocks (∼−28‰) suggests that the carbon was mainly derived from primary phototrophic and/or chemolithoautotrophic producers. The absence of diagenetic pyrite and diagenetic Fe-carbonate in the carbonaceous sedimentary rocks indicates that organic carbon degradation may have proceeded via fermentation processes and possibly via nitrate-reduction (Fig. 12A) (Godfrey and Falkowski, 2009). Occasionally during periods of rapid relative sea level rise, the continental shelf of the trailing margin basin became completely drowned, resulting in shelf conditions that were starved with respect to siliciclastic input. It was during these periods that iron-enriched hydrothermal plume water upwelled onto the shelf to form laterally continuous beds of magnetic mudstone and banded iron formation (Beukes and Cairncross, 1991; Smith, 2007). It was probably during this stage that the Witwatersrand-Mozaan basin achieved its maximum areal extent – far beyond the presently preserved structural limit of the basin (Fig. 2A) (Myers et al., 1990; Beukes and Cairncross, 1991; Beukes, 1995; Beukes and Nelson, 1995). Such a transgressive event is preserved in the lower Parktown Formation, where an iron-enriched hydrothermal plume upwelled over and onto carbonaceous mudstone of the proximal marine depofacies. The resultant formation of $^{13}C_{carb}$-depleted Mn-bearing Fe-carbonate concretions is seen as a direct consequence of this event and may signal very low concentrations of free oxygen in basin water at this time (e.g., Cochrane, 2009). The possibility that Mn-oxyhydroxides were present in the environment is supported by the high Co concentrations (up to 1.8 wt.%) measured from diagenetic pyrite in carbonate facies BIF in the Hospital Hill Subgroup (Guy et al., 2010). These anomalous concentrations of Co were tentatively linked to the reductive dissolution of Fe–Mn-oxyhydroxides during diagenesis (Guy et al., 2010). Interestingly, rare pyrite in the carbonate facies BIF displays more ^{34}S-enriched $\delta^{34}S$ values (+5 to +7‰) than pyrite from magnetic mudstone and oxide facies BIF, which plot near the ARA (Fig. 9B). Considering the negative $\Delta^{33}S$–$\delta^{34}S$ correlation observed from samples from the Hospital Hill Subgroup (Fig. 9B), the more ^{34}S-enriched $\delta^{34}S$ values from the carbonate facies BIF might indicate the incorporation of a mass-dependent oceanic-derived sulfate component (∼+12‰; Ueno et al., 2008). Sequestration of the sulfate reservoir might have been aided by the presence of an organic substrate, which was subsequently degraded into carbonate by the Fe- and Mn-oxyhydroxide reducers (Figs. 9B and 12A).

From a basinal perspective, the occurrence of positive $\Delta^{33}S$ values in both proximal and distal marine depofacies implies that the water column must have been highly depleted in sulfate. This is supported by the presence of diagenetic Fe–Mn carbonates, extremely low S/C ratios, absence of early diagenetic pyrite and high organic carbon content (Fig. 5). However, in more detail there is a clear trend for $\Delta^{33}S$ values in distal shelf iron formations to be more positive in relation to proximal carbonaceous mudstones

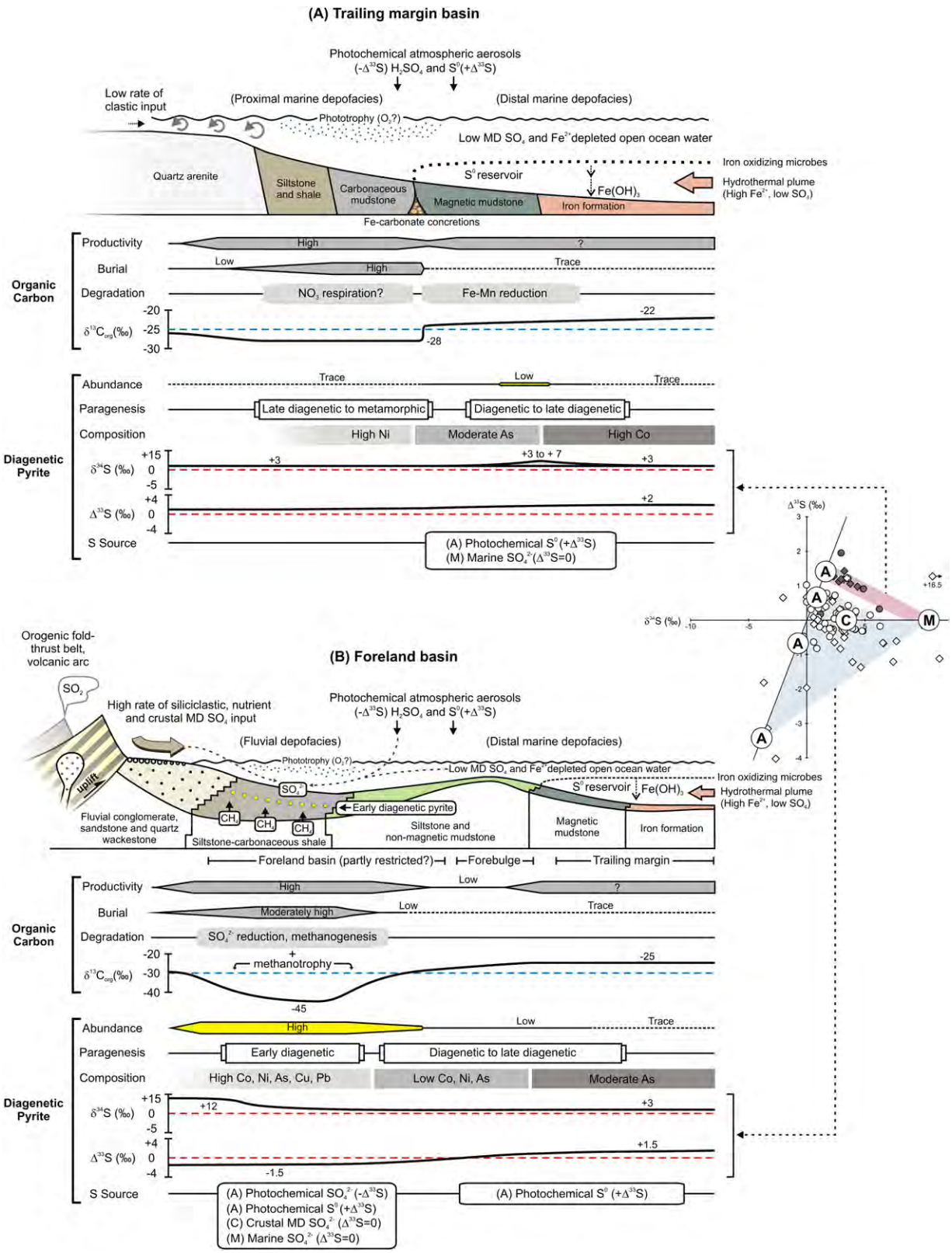

Fig. 12. Depositional models for (A) the trailing margin basin of the Hospital Hill Subgroup and (B) the foreland basin of the Government Subgroup. Note that with rapid subsidence and sea level rise, open marine ± hydrothermal plume water invaded the foreland basin. Fluvial deposition was interrupted by three putative glacial events.

(Fig. 12A). This trend can be explained by either the rapid sequestration of the reduced photochemical reservoir in Fe-rich sedimentary rocks (e.g., Ono et al., 2009a,b) and/or that the diminished signatures in the carbonaceous mudstones reflect later generations of diagenetic or epigenetic pyrite (Fig. 12A).

7.2. Foreland basin setting of the Government and Jeppestown subgroups

Sequence stratigraphic analyses and basin reconstruction of the West Rand Group reveal that the middle and upper parts of the

West Rand Group were deposited in a foreland basin ahead of an advancing fold and thrust mountain belt to the west and/or northwest, coupled with a trailing margin basin to the southeast of a peripheral bulge (Fig. 12B) (Beukes, 1995). The base of the Government Subgroup (i.e., the Promise Formation) rests paraconformably on the Bonanza Formation in the western parts of the basin, but unconformably on the stratigraphically lower Brixton Formation in the central and eastern parts of the basin (Beukes, 1995; SACS, 2006) (Fig. 3). The differential preservation of strata was interpreted as low angle flexuring in response to foreland basin tectonics (Beukes, 1995). This interpretation is supported by the supposed age of terrane collision between the Kimberley and Witwatersrand blocks at ca. 2.93 Ga, i.e., the age of the lower Government Subgroup (Beukes and Nelson, 1995; Schmitz et al., 2004). As a result of increased tectonism, the source area shifted towards the northwest and depositional styles changed from essentially marine in the preceding Hospital Hill Subgroup to mixed fluvial-marine in the Government and Jeppestown subgroups (Watchorn, 1981; Beukes, 1995). The deposition of immature sedimentary rock types, abundance of soft-sediment deformation, and the presence of disconformable lithological contacts are symptomatic of rapid sediment deposition, negligible reworking and tectonic instability (Watchorn, 1981; Beukes, 1995). Tectonic uplift would have facilitated in the delivery of siliclastic components, dissolved nutrients (transition metals, phosphorus) and sulfur into the basinal environment (Hoffman and Grotzinger, 1992; Beukes, 1995; Konhauser, 2007; Campbell and Allen, 2008). The effects of this chemical influx, specifically sulfur, are reflected by the appearance of early diagenetic pyrite (Guy et al., 2010), negative $\Delta^{33}S$ values and highly ^{13}C-depleted organic carbon in the fluvial-dominated depofacies adjacent to the orogenic terrane/volcanic arc (Figs. 7A, 9A, C, D and 12B). Together, these geochemical signatures probably represent the products of a syntrophic relationship between sulfate reducers and anaerobic methanotrophs along a methane-sulfate transition zone (DeLong, 2000; Orphan et al., 2001). This relationship would explain the limited preservation of organic carbon in the fluvial-dominated depofacies, the covariance between sulfur and organic carbon (Fig. 5C) and possibly, the cause of the three glacial episodes in the Government Subgroup. A crustal source of the sulfur influx was initially proposed due to the spatial association between trace-element-rich early diagenetic pyrite (e.g., Ni, Co and As) and fluvial braidplain deposits, and their dual connection with a foreland basin tectonic setting (Guy et al., 2010). This earlier suggestion is coherent with the multiple sulfur isotope results obtained during this study and may also explain the preponderance of reworked fragments of sedimentary pyrite in the auriferous quartz-pebble conglomerates of the Central Rand Group (Hofmann et al., 2009; Guy, 2012). Although the precise origin of the inferred crustal sulfur reservoir is not immediately apparent, it may be related to subaerial volcanism (Kump and Barley, 2007; Gaillard et al., 2011) and/or low temperature geothermal systems (McCarthy et al., 1990; Myers et al., 1990; Falconer, 2003) and/or weathering of reactive sulfide minerals in the hinterland, e.g., pyrrhotite (Reinhard et al., 2009; Lefticariu et al., 2010; Wacey et al., 2011). Mixing between these various sulfur reservoirs may have produced a crustal sulfur reservoir characterized by small $\Delta^{33}S$ anomalies and $\delta^{34}S$ values between 0 and +10‰ (Chaussidon et al., 1989; Ohmoto and Goldhaber, 1997). The partial restriction of the basin behind the foreland bulge could also have led to higher concentrations of dissolved sulfur in the basin, especially at times of relatively low stands of sea level (e.g., the lower Coronation and Rietkuil formations). Thus, the ambient water in the foreland basin consisted of sulfur that was predominantly derived from a mass-dependent crustal reservoir ($\delta^{34}S = \sim+3$ to +5‰), with lesser inputs from a mass-independent photochemical reservoir (i.e., data points along the ARA) and a mass-dependent seawater reservoir ($\delta^{34}S = \sim+10$ to +12‰; Ueno et al., 2008) (Figs. 9D and 12B).

It is important to stress that in the distal parts of the foreland basin (e.g., AM1 drill-core) and in the direction of the Mozaan basin, distal marine sedimentation prevailed. In a similar manner to the Hospital Hill Subgroup, Fe-enriched hydrothermal plume waters occasionally transgressed into the foreland basin during periods of rapid sea level rise (e.g., Silverfields iron formation in the Coronation Formation). Depositional facies tracts and geochemical signatures of the distal marine depofacies in the Government and Jeppestown subgroups are very similar to those of the distal marine depofacies of the underlying Hospital Hill Subgroup and much of the same sedimentary and diagenetic conditions and processes must have occurred (Fig. 12A and B). However, there are two major differences. First, the magnitudes of the positive $\Delta^{33}S$ anomalies in the foreland basin are attenuated by almost half relative to the $\Delta^{33}S$ anomalies in the Hospital Hill Subgroup (Figs. 9B and 12). Second, the negative $\Delta^{33}S$–$\delta^{34}S$ correlation intersects the $\delta^{34}S$ axis at a value between +3 and +5‰ in the foreland basin, in comparison to ~+12‰ in the Hospital Hill Subgroup (Figs. 9B and 12). The lowering of the $\delta^{34}S$ and $\Delta^{33}S$ intercepts in the foreland basin tectonic setting is most probably related to mixing with the crustal sulfur reservoir, as described above.

8. Conclusion

Multiple sulfur and organic carbon isotope ratios were measured from non-conglomeratic sedimentary rocks of the ca. 3.0–2.8 Ga Witwatersrand Supergroup to investigate the occurrence of small $\Delta^{33}S$ anomalies (±2‰) during the Mesoarchean Era and their potential link to diamictite deposits on the Kaapvaal Craton (e.g., Ono et al., 2006a,b,c). In contrast to previous studies, a large number of lithologically diverse rock samples were collected from different geographic locales in the basin (proximal to distal depofacies) and from virtually all shale-bearing intervals in the Witwatersrand Supergroup. In addition, detailed petrographic and mineral chemical analyses were conducted on pyrite to distinguish the different pyrite generations and to better constrain the paragenetic history of pyrite in non-conglomeratic sedimentary rocks. This multifaceted approach removed the masking effects caused by post-depositional alteration (e.g., Fig. 9H) and revealed a more accurate representation of the multiple sulfur and organic isotope record of the Witwatersrand Supergroup.

The emerging picture of the multiple sulfur and organic carbon isotope record illustrates the interplay between Archean atmospheric chemistry, biology and geology. In the marine depositional environments of the tectonically quiescent Hospital Hill Subgroup, seawater sulfate concentrations were very low and rare pyrite contained an elemental sulfur photochemical signature. Carbon cycling probably involved photoautotrophs, methanogens and Fe–Mn reducers. In contrast, the fluvial-dominated depofacies that formed during tectonically active periods of sedimentation contained higher levels of dissolved sulfate – as evidenced by abundant early diagenetic pyrite and the occurrence of small $\Delta^{33}S$ values caused by mixing of a variety of mass-dependent and mass-independent sulfur reservoirs (e.g., crustal, photochemical and marine). Carbon cycling in these environments involved photoautotrophs, methanogens, anaerobic methanotrophs and sulfate reducers.

Numerous hypotheses have been proposed to explain the secular reduction of the magnitude of $\Delta^{33}S$ during the Mesoarchean Era (e.g., Ono et al., 2006a; Ohmoto et al., 2006; Farquhar et al., 2007; Domagal-Goldman et al., 2008; Thomazo et al., 2009; Halevy et al., 2010). These hypotheses sought to relate the $\Delta^{33}S$ record with changes in atmospheric chemistry. However, the results from

this study suggest that the small magnitudes of the $\Delta^{33}S$ anomalies in the Witwatersrand Supergroup are primarily due to dilution of the atmospheric signature by mass-dependent crustal sulfur (e.g., subaerial volcanism, pyrite weathering). Indeed, the input of crustal sulfur into the basin environment may have played an important role in ushering in the Mesoarchean glaciations – which paradoxically, might also explain the presence of large magnitude $\Delta^{33}S$ anomalies (−4.0 to +1.3‰) in the diamictite-bearing Coronation Formation (e.g., Fig. 3 of Williford et al., 2011).

Acknowledgments

The authors are grateful to William J. Olszewski at the Massachusetts Institute of Technology and Craig Hebert at the University of Maryland for assisting with sulfur and organic carbon isotope measurements. Two anonymous reviewers and the editor are thanked for their constructive comments on an earlier version of the manuscript. This work is supported by a research grant to NJB by the National Research Foundation, Pretoria (GUN 2053184), a NASA Exobiology grant to SO (NNX07AU12G) and a NASA-NAI grant to MLF (NNA04CC09A). AngloGold Ashanti Ltd., Goldfields Ltd. and the Council for Geoscience, South Africa are gratefully acknowledged for providing access to drill-core.

References

Anbar, A.D., Duan, Y., Lyons, T.W., Arnold, G.L., Kendall, B., Creaser, R.A., Kaufman, A.J., Gordon, G.W., Scott, C., Garvin, J., Buick, R., 2007. A whiff of oxygen before the great oxidation event? Science 317, 1903–1906.

Armstrong, R.A., Compston, W., Retief, E.A., Williams, L.S., Welke, H.J., 1991. Zircon ion microprobe studies bearing on the age and evolution of the Witwatersrand basin. Precambrian Research 53, 243–266.

Bao, H., Rumble, D., Lowe, D.R., 2007. The five stable isotope compositions of Fig Tree barites: implications on sulfur cycle in ca. 3.2 Ga oceans. Geochimica et Cosmochimica Acta 71, 4868–4879.

Bekker, A., Kaufman, A.J., 2007. Oxidative forcing of global climate change: a biogeochemical record across the oldest Paleoproterozoic ice age in North America. Earth and Planetary Science Letters 258, 486–499.

Bekker, A., Holland, H.D., Wang, P.L., Rumble, D., Stein, H.J., Hannah, J.L., Coetzee, L.L., Beukes, N.J., 2004. Dating the rise of atmospheric oxygen. Nature 427, 117–120.

Berner, R.A., Raiswell, R., 1983. Burial of organic carbon and pyrite sulfur in sediment over Phanerozoic time: a new theory. Geochimica et Cosmochimica Acta 47, 855–862.

Berner, R.A., Raiswell, R., 1984. C/S method for distinguishing freshwater from marine sedimentary rocks. Geology 12, 365–368.

Beukes, N.J., 1995. Stratigraphy and basin analysis of the West Rand Group with special reference to prospective areas for placer gold deposits (Unpubl.). Department of Geology, Rand Afrikaans University (University of Johannesburg), 117 pp.

Beukes, N.J., 1996. Sole Marks and combined-flow storm event beds in the Brixton Formation of the siliciclastic Archean Witwatersrand Supergroup, South Africa. Journal of Sedimentary Research 66, 567–576.

Beukes, N.J., Buxton, M., 1992. Genetic stratigraphy of the West Rand Group, Witwatersrand Supergroup: Annual Report, March 1990 to February 1991 (Unpubl.). Department of Geology, Rand Afrikaans University (University of Johannesburg), 60 pp.

Beukes, N.J., Cairncross, B., 1991. A lithostratigraphic–sedimentological reference profile for the Late Archaean Mozaan Group, Pongola Sequence: application to sequence to stratigraphy and correlation with the Witwatersrand Supergroup. South African Journal of Geology 94, 44–69.

Beukes, N.J., Dorland, H., Gutzmer, J., Nedachi, M., Ohmoto, H., 2002. Tropical laterites, life on land, and the history of atmospheric oxygen in the Paleoproterozoic. Geology 30, 491–494.

Beukes, N.J., Gutzmer, J., 2008. Origin and paleoenvironmental significance of major iron formations at the archean-paleoproterozoic boundary. Reviews in Economic Geology 15, 5–47.

Beukes, N.J., Klein, C., 1992. Models for iron-formation deposition. In: Schopf, J.W., Klein, C. (Eds.), The Proterozoic Biosphere. Cambridge University Press, Cambridge, pp. 159–163.

Beukes, N.J., Klein, C., Kaufman, A.J., Hayes, J.M., 1990. Carbonate petrography, kerogen distribution, and carbon and oxygen isotopic variations in an Early Proterozoic transition from limestone to iron-formation deposition, Transvaal Supergroup, South Africa. Economic Geology 85, 663–690.

Beukes, N.J., Lowe, D.R., 1989. Environmental control on diverse stromatolite morphologies in the 3000 Myr Pongola Supergroup, South Africa. Sedimentology 36, 383–397.

Beukes, N.J., Nelson, J.P., 1995. Sea-level fluctuation and basin subsidence controls on the setting of auriferous paleoplacers in the Archean Witwatersrand Supergroup: a genetic and sequence stratigraphic approach. In: Extended Abstract, South African Geocongress, pp. 860–863.

Boetius, A., Ravenschlag, K., Schubert, C.J., Rickert, D., Widdel, F., Gieseke, A., Amann, R., Jorgensen, B.B., Witte, U., Pfannkuche, O., 2000. A marine microbial consortium apparently mediating anaerobic oxidation of methane. Nature 407, 623–626.

Brocks, J.J., Logan, G.A., Buick, R., Summons, R.E., 1999. Archean molecular fossils and the early rise of eukaryotes. Science 285, 1033–1036.

Buick, R., 2008. When did oxygenic photosynthesis evolve? Philosophical Transactions of the Royal Society 363, 2731–2743.

Cairncross, B., Beukes, N.J., Gutzmer, J., 1997. The Manganese Adventure: The South African Manganese Fields. Associated Ore and Metal Corporation, Ltd., Johannesburg, Republic of South Africa.

Camden-Smith, P.M., 1980. The sedimentology, geochemistry, and diagenesis of the West Rand Group sediments in the Heidelberg Area. M. Sc. Thesis (Unpubl.), University of Cape Town, 232 pp.

Campbell, I.H., Allen, C.M., 2008. Formation of supercontinents linked to increases in atmospheric oxygen. Nature Geoscience 1, 554–558.

Canfield, D.E., Raiswell, R., Westrich, J.T., Reaves, C.M., Berner, R.A., 1986. The use of chromium reduction in the analysis of reduced inorganic sulfur in sediments and shales. Chemical Geology 54, 149–155.

Cates, N.L., Mojzsis, S.J., 2006. Chemical and isotopic evidence for widespread Eoarchean sedimentary enclaves in southern West Greenland. Geochimica et Cosmochimica Acta 71, 5862–5875.

Catuneanu, O., 2001. Flexural partitioning in the Late Archaean Witwatersrand foreland system. South Africa. Sedimentary Geology 141/142, 95–112.

Chaussidon, M., Albarede, F., Sheppard, S.M.F., 1989. Sulphur isotope variations in the mantle from ion microprobe analyses of micro-sulphide inclusions. Earth and Planetary Science Letters 92, 144–156.

Cloud, P., 1972. A working model of the primitive Earth. American Journal of Science 272, 537–548.

Cochrane, J.M., 2009. Diagenetic carbonates and biogeochemical cycling of organic matter in selected Archean-Paleoproterozoic sedimentary successions of the Kaapvaal Craton, South Africa. M. Sc. Thesis (Unpubl.), University of Johannesburg, 139 pp.

Coward, M.P., Spencer, R.M., Spencer, C.E., 1995. Development of the Witwatersrand Basin, South Africa. In: Coward, M.P., Ries, A.C. (Eds.), Early Precambrian Processes. Geological Society, London, pp. 243–269, Special Publications 95.

DeLong, E.F., 2000. Resolving a methane mystery. Nature 407, 577–579.

Des Marais, D.J., 2000. When did photosynthesis emerge on Earth? Science 289, 1703–1705.

Des Marais, D.J., 2001. Isotopic evolution of the biogeochemical carbon cycle during the Precambrian. In: Valley, J.W., Cole, D.R. (Eds.), Stable Isotope Geochemistry. Mineralogical Society of America, Washington, DC.

Domagal-Goldman, S.D., Kasting, J.F., Johnston, D.T., Farquhar, J., 2008. Organic haze, glaciations and multiple sulfur isotopes in the Mid-Archean Era. Earth and Planetary Science Letters 269, 29–40.

Eigenbrode, J.L., Freeman, K.H., 2006. Late Archean rise of aerobic microbial ecosystems. Proceedings of the National Academy of Sciences of the United States of America 103, 15759–15764.

Eigenbrode, J.L., Freeman, K.H., Summons, R.E., 2008. Methylhopane biomarker hydrocarbons in Hamersley Province sediments provide evidence for Neoarchean aerobiosis. Earth and Planetary Science Letters 273, 323–331.

Eriksson, K.A., Turner, B.R., Vos, R.G., 1981. Evidence of tidal processes from the lower part of the Witwatersrand Supergroup, South Africa. Sedimentary Geology 29, 309–325.

Evans, D.A.D., 2003. A fundamental Precambrian–Phanerozoic shift in Earth's glacial style? Tectonophysics 375, 353–385.

Eyles, N., 1993. Earth's glacial record and its tectonic setting. Earth-Science Reviews 35, 1–248.

Falconer, D.M., 2003. Sediment-hosted gold and sulphide mineralization, Belle Brook, Southland, New Zealand. M. Sc. Thesis (Unpubl.), University of Otago, 373 pp.

Farquhar, J., Wing, B.A., 2003. Multiple sulfur isotopes and the evolution of the atmosphere. Earth and Planetary Science Letters 213, 1–13.

Farquhar, J., Bao, H., Thiemans, M., 2000. Atmospheric influence of Earth's earliest sulfur cycle. Science 289, 756–758.

Farquhar, J., Peters, M., Johnston, D.T., Strauss, H., Masterson, A., Wiechert, U., Kaufman, A.J., 2007. Isotopic evidence for Mesoarchaean anoxia and changing atmospheric sulphur chemistry. Nature 449, 706–709.

Farquhar, J., Savarino, J., Airieau, S., Thiemens, M.H., 2001. Observation of wavelength-sensitive mass-independent sulfur isotope effects during SO_2 photolysis: implications for the early atmosphere. Journal of Geophysical Research 106, 1–11.

Farquhar, J., Wing, B.A., McKeegan, K.D., Harris, J.W., Cartigny, P., Thiemens, M.H., 2002. Mass-independent sulfur of inclusions in diamond and sulfur recycling on early Earth. Science 298, 2369–2372.

Fleet, M.E., 1998. Detrital pyrite in Witwatersrand gold reefs: X-ray diffraction evidence and implications for atmospheric evolution. Terra Nova 10, 302–306.

Frimmel, H.E., Groves, D.I., Kirk, J., Ruiz, J., Chesley, J., Minter, W.E.L., 2005. The formation and preservation of the Witwatersrand Goldfields, the World's largest gold province. In: Economic Geology 100th Anniversary Volume, pp. 769–797.

Gaillard, F., Scaillet, B., Arndt, N.T., 2011. Atmospheric oxygenation caused by a change in volcanic degassing pressure. Nature 478, 229–232.

Godfrey, L.V., Falkowski, P.G., 2009. The cycling and redox state of nitrogen in the Archean ocean. Nature Geoscience 2, 725–729.

Grandstaff, D.E., 1980. Origin of uraniferous conglomerates at Elliott Lake, Canada and Witwatersrand, South Africa: implications for oxygen in the Precambrian atmosphere. Precambrian Research 13, 1–26.
Guo, Q., Strauss, H., Schröder, S., Gutzmer, J., Wing, B.A., Baker, M.A., Kaufman, A.J., Kim, S.T., Farquhar, J., 2009. Reconstructing Earth's surface oxidation across the Archean-Proterozoic transition. Geology 37, 399–402.
Gutzmer, J., Nhleko, N., Beukes, N.J., Pickard, A., Barley, M.E., 1999. SHRIMP age of a quartz porphyry sill in the Mozaan group: geochronological implication for the Pongola and the Witwatersrand Supergroups. South African Journal of Geology 102, 139–146.
Guy, B.M., 2012. Pyrite in the Mesoarchean Witwatersrand Supergroup. Ph.D. Thesis (Unpubl.), University of Johannesburg, 492 pp.
Guy, B.M., Beukes, N.J., Gutzmer, J., 2010. Paleoenvironmental controls on the texture and chemical composition of pyrite from non-conglomeratic sedimentary rocks of the Mesoarchean Witwatersrand Supergroup, South Africa. South African Journal of Geology 113, 195–228.
Habicht, K.S., Gade, M., Thamdrup, B., Berg, P., Canfield, D.E., 2002. Calibration of sulfate levels in the Archean ocean. Science 298, 2372–2374.
Halevy, I., Johnston, D.T., Schrag, D.P., 2010. Explaining the structure of the Archean mass-independent sulfur isotope record. Science 329, 204–207.
Hayes, J.M., 1983. Geochemical evidence bearing on the origin of aerobiosis, a speculative hypothesis. In: Schopf, J.W. (Ed.), Earth's Earliest Biosphere: Its Origin and Evolution. Princeton University Press, Princeton, pp. 291–301.
Hayes, J.M., 1994. Global methanotrophy at the Archean–Proterozoic transition. In: Bengtson, S. (Ed.), Early Life on Earth (Nobel Symposium 84). Columbia University Press, New York, pp. 220–236.
Hegner, E., Kröner, A., Hunt, P., 1994. A precise U–Pb zircon age for the Archaean Pongola Supergroup volcanics in Swaziland. Journal of African Earth Sciences 18, 339–341.
Hinrichs, K.-U., 2002. Microbial fixation of methane carbon at 2.7 Ga: was an anaerobic mechanism possible? Geochemistry Geophysics Geosystems 3, 1042, http://dx.doi.org/10.1029/2001GC000286.
Hinrichs, K.-U., Hayes, J.M., Sylva, S.P., Brewer, P.G., DeLong, E.F., 1999. Methane-consuming archaebacteria in marine sediments. Nature 398, 802–805.
Hoffman, P.F., Grotzinger, J.P., 1992. Orographic precipitation, erosional unloading and tectonic style. Geology 21, 195–198.
Hofmann, A., Bekker, A., Rouxel, O., Rumble, D., Master, S., 2009. Multiple sulphur and iron isotope composition of detrital pyrite in Archaean sedimentary rocks: a new tool for provenance analysis. Earth and Planetary Science Letters 286, 436–445.
Holland, H.D., 1984. The Chemical Evolution of the Atmosphere and Oceans. Princeton University Press, Princeton.
Hu, G.X., Rumble, D., Wang, P.L., 2003. An ultraviolet laser microprobe for the in situ analysis of multisulfur isotopes and its use in measuring Archean sulfur isotope mass-independent anomalies. Geochimica et Cosmochimica Acta 67, 3101–3118.
Hurtgen, M.T., Arthur, M.A., Halverson, G.P., 2005. Neoproterozoic sulfur isotopes, the evolution of microbial sulfur species, and the burial efficiency of sulfide as sedimentary pyrite. Geology 33, 41–44.
Hurtgen, M.T., Arthur, M.A., Suits, N.S., Kaufman, A.J., 2002. The sulfur isotopic composition of Neoproterozoic seawater sulfate: implications for a snowball Earth? Earth and Planetary Science Letters 203, 413–430.
Johnston, D.T., 2011. Multiple sulfur isotopes and the evolution of Earth's surface sulfur cycle. Earth Science Reviews 106, 161–183.
Johnston, D.T., Poulton, S.W., Fralick, P.W., Wing, B.A., Canfield, D.E., Farquhar, J., 2006. Evolution of the oceanic sulphur cycle at the end of the Paleoproterozoic. Geochimica et Cosmochimica Acta 70, 5723–5739.
Johnston, D.T., Wing, B.A., Farquhar, J., Kaufman, A.J., Strauss, H., Lyons, T.W., Kah, L.C., Canfield, D.E., 2005. Active microbial sulphur disproportionation in the Mesoproterozoic. Science 310, 1477–1479.
Kamber, B.S., Whitehouse, M.J., 2007. Micro-scale sulphur isotope evidence for sulphur cycling in the late Archean shallow ocean. Geobiology 5, 5–17.
Kappler, A., Pasquero, C., Konhauser, K.O., Newman, D.K., 2005. Deposition of banded iron formations by anoxygenic phototrophic Fe(II)-oxidizing bacteria. Geology 33, 865–868.
Karpeta, W.P., Els, B.G., 1999. The auriferous Late Archaean Central Rand Group of South Africa: sea-level control of sedimentation? Precambrian Research 97, 191–214.
Kasting, J.F., Holland, H.D., Kump, L.R., 1992. Atmospheric evolution: the rise of oxygen. In: Schopf, J.W., Klein, C. (Eds.), The Proterozoic Biosphere. Cambridge University Press, Cambridge, pp. 159–163.
Kasting, J.F., Howard, M.T., 2006. Atmospheric composition and climate on the early Earth. Philosophical Transactions of the Royal Society 361, 1733–1742.
Kasting, J.F., Ono, S., 2006. Paleoclimates: the first two billion years. Philosophical Transactions of the Royal Society 361, 917–929.
Kaufman, A.J., Johnston, D.T., Farquhar, J., Masterson, A.L., Lyons, T.W., Bates, S., Anbar, A.D., Arnold, G.L., Garvin, J., Buick, R., 2007. Late Archean biospheric oxygenation and atmospheric evolution. Science 317, 1900–1903.
Konhauser, K., 2007. Introduction to Geomicrobiology. Blackwell Publishing, Malden MA.
Kopp, R.E., Kirschvink, J.L., Hilburn, I.A., Nash, C.Z., 2005. The Paleoproterozoic snowball Earth: a climate disaster triggered by the evolution of oxygenic photosynthesis. Proceedings of the National Academy of Sciences of the United States of America 102, 11131–11136.
Kositcin, N., Krapez, B., 2004. SHRIMP U-Pb detrital zircon geochronology of the Late Archaean Witwatersrand Basin of South Africa: relation between zircon provenance age spectra and basin evolution. Precambrian Research 129, 141–168.
Kositcin, N., McNaughton, N.J., Griffin, B.J., Fletcher, I.R., Groves, D.I., Rasmussen, B., 2003. Textural and geochemical discrimination between xenotime of different origin in the Archaean Witwatersrand Basin, South Africa. Geochimica et Cosmochimica Acta 67, 709–731.
Kump, L.R., Barley, M.E., 2007. Increased subaerial volcanism and the rise of atmospheric oxygen 2.5 billion years ago. Nature 448, 1033–1036.
Law, J.D.M., Phillips, G.N., 2005. Hydrothermal replacement model for Witwatersrand gold. In: Economic Geology 100th Anniversary Volume, pp. 799–811.
Lefticariu, L., Pratt, L.A., LaVerne, J.A., Schimmelmann, A., 2010. Anoxic pyrite oxidation by water radiolysis products—a potential source of biosustaining energy. Earth and Planetary Science Letters 292, 57–67.
McCarthy, T.S., Stanistreet, I.G., Cadle, A.B., Durrheim, R., 1990. The geology of the Ventersdorp Supergroup (Bezuidenhout Valley) outlier to the east of Johannesburg and its relevance to the tectonics of a Witwatersrand Basin margin. South African Journal of Geology 93, 289–309.
McCrea, J.M., 1950. On the isotopic chemistry of carbonates and a paleotemperature scale. Journal of Chemical Physics 18, 849–857.
Meyer, F.M., Tainton, S., Saager, R., 1990. The mineralogy and geochemistry of small-pebble conglomerates from the Promise Formation in the West Rand and Klerksdorp areas. South African Journal of Geology 93, 118–134.
Mojzsis, S.J., Coath, C.D., Greenwood, J.P., McKeegan, K.D., Harrison, T.M., 2003. Mass-independent isotope effects in Archean (2.5 to 3.8 Ga) sedimentary sulfides determined by ion microprobe analysis. Geochimica et Cosmochimica Acta 67, 1635–1658.
Myers, R.E., McCarthy, T.S., Stanistreet, I.G., 1990. A tectono-sedimentary reconstruction of the development and evolution of the Witwatersrand basin, with particular emphasis on the Central Rand Group. South African Journal of Geology 93, 180–201.
Nel, L.T., 1935. The geology of the Klerksdorp-Ventersdorp area: an explanation of the geological map. Special Publications of the Geological Survey of South Africa 9, 1–168.
Nelson, J.P., Beukes, N.J., van Eeden, J., 1995. Sequence stratigraphic and basin analysis of the late Archean Witwatersrand Supergroup. In: Extended Abstract, South African Geocongress, pp. 875–877.
Nhleko, N., 2003. The Pongola Supergroup in Swaziland. Ph.D. Thesis (Unpubl.), Rand Afrikaans University (University of Johannesburg), 298 pp.
Noffke, N., Beukes, N.J., Hazen, R.M., 2006. Microbially induced sedimentary structures in the 2.9 Ga old Brixton Formation, Witwatersrand Supergroup, South Africa. Precambrian Research 146, 35–44.
Noffke, N., Beukes, N.J., Bower, D., Hazen, R.M., Swift, D.J.P., 2008. An actualistic perspective into Archean worlds—(cyano-)bacterially induced sedimentary structures in the siliciclastic Nhlazatse Section, 2.9 Ga Pongola Supergroup, South Africa. Geobiology 6, 5–20.
Ohmoto, H., 2003. Nonredox transformations of magnetite–hematite in hydrothermal systems. Economic Geology 98, 157–161.
Ohmoto, H., Goldhaber, M.B., 1997. Sulfur and carbon isotopes. In: Barnes, H.L. (Ed.), Geochemistry of Hydrothermal Ore Deposits. John Wiley and Sons, New York, pp. 517–611.
Ohmoto, H., Watanabe, Y., Ikemi, H., Poulson, S.R., Taylor, B.E., 2006. Sulphur isotope evidence for an oxic Archaean atmosphere. Nature 442, 908–911.
Ono, S., Beukes, N.J., Rumble, D., 2009a. Origin of two distinct multiple-sulfur isotope compositions of pyrite in the 2.5 Ga Klein Naute Formation, Griqualand West Basin, South Africa. Precambrian Research 169, 48–57.
Ono, S., Beukes, N.J., Rumble, D., Fogel, M.L., 2006a. Early evolution of atmospheric oxygen from multiple-sulfur and carbon isotope records of the 2.9 Ga Mozaan Group of the Pongola Supergroup, Southern Africa. South African Journal of Geology 109, 97–108.
Ono, S., Eigenbrode, J.L., Pavlov, A.A., Kharecha, P., Rumble, D., Kasting, J.F., Freeman, K.H., 2003. New insights into Archean sulfur cycle from mass independent sulfur isotope records from the Hamersley Basin, Australia. Earth and Planetary Science Letters 213, 15–30.
Ono, S., Kaufman, A.J., Farquhar, J., Sumner, D.Y., Beukes, N.J., 2009b. Lithofacies control on multiple-sulfur isotope records and the Neoarchean sulfur cycles. Precambrian Research 169, 58–67.
Ono, S., Shanks, W.C., Rouxel, O., Rumble, D., 2007. S-33 constraints on the seawater sulfate contribution in modern seafloor hydrothermal vent sulfides. Geochimica et Cosmochimica Acta 71, 1170–1182.
Ono, S., Wing, B., Johnston, D., Farquhar, J., Rumble, D., 2006b. Mass-dependent fractionation of quadruple sulfur isotope system as a new tracer of sulfur biogeochemical cycles. Geochimica et Cosmochimica Acta 70, 2238–2252.
Ono, S., Wing, B., Rumble, D., Farquhar, J., 2006c. High precision analysis of all four stable isotopes of sulfur (32S, ^{33}S, ^{34}S and ^{36}S) at nanomole levels using a laser fluorination isotope-ratio-monitoring gas chromatography–mass spectrometry. Chemical Geology 225, 30–39.
Orphan, V.J., House, C.H., Hinrichs, K.-U., McKeegan, K.D., DeLong, E.F., 2001. Methane-consuming Archaea revealed by directly coupled isotopic and phylogenetic analysis. Science 293, 484–487.
Papineau, D., Mojzsis, S.J., Coath, C.D., Karhu, J.A., McKeegan, K.D., 2005. Multiple sulfur isotopes of sulfides from sediments in the aftermath of Paleoproterozoic glaciations. Geochimica et Cosmochimica Acta 69, 5033–5060.
Papineau, D., Mojzsis, S.J., Schmitt, A.K., 2007. Multiple sulfur isotopes from Paleoproterozoic Huronian interglacial sediments and the rise of atmospheric oxygen. Earth and Planetary Science Letters 255, 188–212.

Partridge, M.A., Golding, S.D., Baublys, K.A., Young, E., 2008. Pyrite paragenesis and multiple sulfur isotope distribution in late Archean and early Paleoproterozoic Hamersley Basin sediments. Earth and Planetary Science Letters 272, 41–49.
Pavlov, A.A., Kasting, J.F., 2002. Mass-independent fractionation of sulfur isotopes in Archean sediments: strong evidence for an anoxic Archean atmosphere. Astrobiology 2, 27–41.
Philippot, P., Van Zuilen, M., Lepot, K., Thomazo, C., Farquhar, J., Van Kranendonk, M.J., 2007. Early Archaean microorganisms preferred elemental sulphur, not sulfate. Science 317, 1534–1537.
Phillips, G.N., Law, J.D.M., 2000. Witwatersrand gold fields: geology, genesis and exploration. Society of Economic Geologists Reviews 13, 439–500.
Poujol, M., Robb, L.J., Anhaeusser, C.R., Gericke, B., 2003. A review of the geochronological constraints on the evolution of the Kaapvaal Craton, South Africa. Precambrian Research 127, 181–213.
Raiswell, R., Berner, R.A., 1986. Pyrite and organic matter in Phanerozoic normal marine shales. Geochimica et Cosmochimica Acta 50, 1967–1976.
Reinhard, C.T., Raiswell, R., Scott, C., Anbar, A.D., Lyons, T.W., 2009. A late Archean sulfidic sea stimulated by early oxidative weathering of the continents. Science 326, 713–716.
Ries, J.B., Fike, D.A., Pratt, L.M., Lyons, T.W., Grotzinger, J.P., 2009. Superheavy pyrite ($\delta^{34}S_{pyr} > \delta^{34}S_{CAS}$) in the terminal Proterozoic Nama Group, southern Namibia: a consequence of low seawater sulfate at the dawn of animal life. Geology 37, 743–746.
SACS (South African Committee for Stratigraphy), 2006. A revised stratigraphic framework for the Witwatersrand Supergroup. Council of Geoscience, Lithostratigraphic Series 42, 1–7.
Savarino, J., Romero, A., Cole-Dai, J., Bekki, S., Thiemens, M.H., 2003. UV induced mass-independent sulfur isotope fractionation in stratospheric volcanic sulfate. Geophysical Research Letters 30, Cite ID 2131.
Schidlowski, M., 2001. Carbon isotopes as biogeochemical recorders of life over 3.8 Ga of Earth history: evolution of a concept. Precambrian Research 106, 117–134.
Schidlowski, M., Hayes, J.M., Kaplan, I.R., 1983. Isotopic inferences of ancient biochemistries: carbon, sulfur, hydrogen and nitrogen. In: Schopf, J.W. (Ed.), Earth's Earliest Biosphere: Its Origin and Evolution. Princeton University Press, Princeton, pp. 149–186.
Schmitz, M.D., Bowring, S.A., de Wit, M.J., Gartz, V., 2004. Subduction and terrane collision stabilize the western Kaapvaal craton tectosphere 2.9 billion years ago. Earth and Planetary Science Letters 222, 363–376.
Schwab, V., Spangenberg, J.E., Grimalt, J.O., 2005. Chemical and carbon isotopic evolution of hydrocarbons during prograde metamorphism from 100 °C to 550 °C: case study in the Liassic black shale formation of Central Swiss Alps. Geochimica et Cosmochimica Acta 69, 1825–1840.
Shen, B., Xiao, S., Kaufman, A.J., Bao, H., Zhou, C., Wang, H., 2008. Stratification and mixing of a post-glacial Neoproterozoic ocean: evidence from carbon and sulfur isotopes in a cap dolostone from northwest China. Earth and Planetary Science Letters 265, 209–228.
Shen, Y., Buick, R., Canfield, D.E., 2001. Isotopic evidence for microbial sulphate reduction in the early Archaean era. Nature 410, 77–81.
Smith, B., 2007. The Paleo-environmental significance of the iron formations and iron-rich Mudstones of the Mesoarchean Witwatersrand-Mozaan Basin, South Africa. M.Sc. Thesis (Unpubl.), University of Johannesburg, 207 pp.
Strauss, H., Des Marais, D.J., Summons, R.E., Hayes, J.M., 1992. The carbon isotopic record. In: Schopf, J.W., Klein, C. (Eds.), The Proterozoic Biosphere. Cambridge University Press, Cambridge, pp. 117–128.
Summons, R.E., Bradley, A.S., Jahnke, L.L., Waldbauer, J.R., 2006. Steroids, triterpenoids and molecular oxygen. Philosophical Transactions of the Royal Society of London Series B-Biological Sciences 361, 951–968.
Summons, R.E., Jahnke, L.L., Hope, J.M., Logan, G.A., 1999. 2-Methylhopanoids as biomarkers for cyanobacterial oxygenic photosynthesis. Nature 400, 554–557.
Tainton, S., Meyer, F.M., 1990. The stratigraphy and sedimentology of the promise formation of the Witwatersrand Supergroup in the western Transvaal. South African Journal of Geology 93, 103–117.
Tankard, A.J., Jackson, M.P.A., Eriksson, K.A., Hobday, D.K., Hunter, D.R., Minter, W.E.L., 1982. Crustal Evolution of Southern Africa, 3.8 Billion Years of Earth History. Springer-Verlag, New York.
Thomazo, C., Ader, M., Farquhar, J., Philippot, P., 2009. Methanotrophs regulated atmospheric sulfur isotope anomalies during the Late Archean (Tumbiana Formation, Western Australia). Earth and Planetary Science Letters 279, 65–75.
Tice, M.M., Lowe, D.R., 2006a. Hydrogen-based carbon fixation in the earliest known photosynthetic organisms. Geology 34, 37–40.
Tice, M.M., Lowe, D.R., 2006b. The origin of carbonaceous matter in pre-3.0 Ga greenstone terrains: a review and new evidence from the 3.42 Ga Buck Reef Chert. Earth-Science Reviews 76, 259–300.
Ueno, Y., Johnson, M.S., Danielache, S.O., Eskebjerg, C., Pandey, A., Yoshida, N., 2009. Geological sulfur isotopes indicate elevated OCS in the Archean atmosphere, solving faint young sun paradox. Proceedings of the National Academy of Sciences of the United States of America 106, 14784–14789.
Ueno, Y., Ono, S., Rumble, D., Maruyama, S., 2008. Quadruple sulfur isotope analysis of ca. 3.5 Ga dresser formation: new evidence for microbial sulfate reduction in the Early Archean. Geochimica et Cosmochimica Acta 72, 5675–5691.
von Brunn, V., Gold, D.J.C., 1993. Diamictite in the Archean Pongola sequence of southern Africa. Journal of African Earth Science 16, 367–374.
Wacey, D., Saunders, M., Brasier, M.D., Kilburn, M.R., 2011. Earliest microbially mediated pyrite oxidation in ~3.4 billion-year-old sediments. Earth and Planetary Science Letters 301, 393–402.
Walther, J., 1894. Einleitung in die Geologisch Historische Wissenschaft, Bd 3, Lithogenesis der Gegenwart. Fischer-Verlag, Jena, pp. 535–1055.
Watanabe, Y., Naraoka, H., Wronkiewicz, D.J., Condie, K.C., Ohmoto, H., 1997. Carbon, nitrogen, and sulfur geochemistry of Archean and Proterozoic shales from the Kaapvaal Craton, South Africa. Geochimica et Cosmochimica Acta 61, 3441–3459.
Watchorn, M.B., 1981. The stratigraphy and sedimentology of the West Rand Basin in the Western Transvaal. Ph.D. Thesis (Unpubl.), University of the Witwatersrand, 154 pp.
Watchorn, M.B., O'Brien, M.F., 1991. The significance of marine modification in some Witwatersrand placers—an example from the Lower Witwatersrand West Rand Group. South African Journal of Geology 94, 333–339.
Whitehouse, M.J., Kamber, B.S., Fedo, C.M., Lepland, A., 2005. Integrated Pb and S–isotope investigation of sulphide minerals from the early Archaean of southwest Greenland. Chemical Geology 222, 112–131.
Williford, K.H., van Kranendonk, M.J., Ushikubo, T., Kozdon, R., Valley, J.W., 2011. Constraining atmospheric oxygen and seawater sulfate concentrations during Paleoproterozoic glaciation: in situ sulfur three-isotope microanalysis of pyrite from the Turee Creek Group, Western Australia. Geochimica et Cosmochimica Acta 75, 5686–5705.
Young, G.M., von Brunn, V., Gold, D.J.C., Minter, W.E.L., 1998. Earths oldest reported glaciation: physical and chemical evidence from the Archean Mozaan Group (~2.9 Ga) of South Africa. Journal of Geology 106, 523–538.
Zahnle, K.J., Claire, M.W., Catling, D.C., 2006. The loss of mass-independent fractionation in sulfur due to a Palaeoproterozoic collapse of atmospheric methane. Geobiology 4, 271–283.